A Radio-to-mm Census of Star-forming Galaxies in Protocluster 4C23.56 at Z = 2.5

The Astrophysical Journal, 842:55 (23pp), 2017 June 10 https://doi.org/10.3847/1538-4357/aa74c2

A Radio-to-mm Census of Star-forming Galaxies in Protocluster 4C23.56 at $Z = 2.5$: Gas Mass and Its Fraction Revealed with ALMA

Minju M. Lee[1,2], Ichi Tanaka[3], Ryohei Kawabe[1,2,4], Kotaro Kohno[5,6], Tadayuki Kodama[4,7], Masaru Kajisawa[8,9], Min S. Yun[10], Kouichiro Nakanishi[2,4], Daisuke Iono[2,4], Yoichi Tamura[5,18], Bunyo Hatsukade[5], Hideki Umehata[5,11], Toshiki Saito[1,2], Takuma Izumi[3], Itziar Aretxaga[12], Ken-ichi Tadaki[3], Milagros Zeballos[12,14], Soh Ikarashi[15], Grant W. Wilson[10], David H. Hughes[12], and R. J. Ivison[16,17]

[1] Department of Astronomy, The University of Tokyo, 7-3-1 Hongo, Bunkyo-ku, Tokyo 133-0033, Japan; minju.lee@nao.ac.jp
[2] National Astronomical Observatory of Japan, 2-21-1 Osawa, Mitaka, Tokyo 181-0015, Japan
[3] Subaru Telescope, National Astronomical Observatory of Japan, 650 North Aohoku Place, Hilo, HI 96720, USA
[4] SOKENDAI (The Graduate University for Advanced Studies), 2-21-1 Osawa, Mitaka, Tokyo 181-0015, Japan
[5] Institute of Astronomy, The University of Tokyo, 2-21-1 Osawa, Mitaka, Tokyo, 181-0015, Japan
[6] Research Center for the Early Universe, The University of Tokyo, 7-3-1 Hongo, Bunkyo, Tokyo 113-0033, Japan
[7] Optical and Infrared Astronomy Division, National Astronomical Observatory of Japan, Mitaka, Tokyo, 181-8588, Japan
[8] Graduate School of Science and Engineering, Ehime University, Bunkyo-cho, Matsuyama 790-8577, Japan
[9] Research Center for Space and Cosmic Evolution, Ehime University, Bunkyo-cho, Matsuyama 790-8577, Japan
[10] Department of Astronomy, University of Massachusetts, Amherst, MA 01003, USA
[11] The Open University of Japan, 2-11 Wakaba, Mihama-ku, Chiba 261-8586, Japan
[12] Instituto Nacional de Astrofisica, Optica y Electronica (INAOE), Aptdo. Postal 51 y 216, 72000 Puebla, Mexico
[13] Max-Planck-Institut fuer extraterrestrische Physik, Postfach 1312, D-85741 Garching, Germany
[14] Instituto Tecnologico Superior de Tlaxco, Predio Cristo Rey Ex-Hda de Xalostoc s/n, 90250 Tlaxcala, Mexico
[15] Kapteyn Astronomical Institute, University of Groningen, P.O. Box 800, 9700 AV Groningen, The Netherlands
[16] Institute for Astronomy, University of Edinburgh, Royal Observatory, Blackford Hill, Edinburgh EH9 3HJ, UK
[17] European Southern Observatory, Karl-Schwarzschild-Str. 2, D-85748 Garching, Germany
[18] Division of Particle and Astrophysical Science, Graduate School of Science, Nagoya University, Furo-cho, Chikusa-ku, Nagoya 464-8602, Japan
Received 2017 February 16; revised 2017 May 2; accepted 2017 May 19; published 2017 June 14

Abstract

We investigate gas contents of star-forming galaxies associated with protocluster 4C23.56 at $z = 2.49$ by using the redshifted CO (3–2) and 1.1 mm dust continuum with the Atacama Large Millimeter/submillimeter Array. The observations unveil seven CO detections out of 22 targeted Hα emitters (HAEs) and four out of 19 in 1.1 mm dust continuum. They have high stellar mass ($M_\star > 4 \times 10^{10}\ M_\odot$) and exhibit a specific star-formation rate typical of main-sequence star-forming galaxies at $z \sim 2.5$. Different gas-mass estimators from CO (3–2) and 1.1 mm yield consistent values for simultaneous detections. The gas mass ($M_{\rm gas}$) and gas fraction ($f_{\rm gas}$) are comparable to those of field galaxies, with $M_{\rm gas} = [0.3, 1.8] \times 10^{11} \times (\alpha_{\rm CO}/(4.36 \times A(Z)))\ M_\odot$, where $\alpha_{\rm CO}$ is the CO-to-H_2 conversion factor and $A(Z)$ is the additional correction factor for the metallicity dependence of $\alpha_{\rm CO}$, and $\langle f_{\rm gas}\rangle = 0.53 \pm 0.07$ from CO (3–2). Our measurements place a constraint on the cosmic gas density of high-z protoclusters, indicating that the protocluster is characterized by a gas density higher than that of the general fields by an order of magnitude. We found $\rho(H_2) \sim 5 \times 10^9\ M_\odot\ {\rm Mpc}^{-3}$ with the CO(3–2) detections. The five ALMA CO detections occur in the region of highest galaxy surface density, where the density positively correlates with global star-forming efficiency (SFE) and stellar mass. Such correlations possibly indicate a critical role of the environment on early galaxy evolution at high-z protoclusters, though future observations are necessary for confirmation.

Key words: galaxies: clusters: general – galaxies: evolution – galaxies: high-redshift – galaxies: ISM – large-scale structure of universe – submillimeter: galaxies

1. Introduction

In the last four decades, it has become clear that galaxy evolution is intertwined with the surrounding environment. Galaxy properties such as star-formation rate, color, and morphology are strongly correlated with projected number densities (e.g., Dressler 1980; Dressler et al. 1997; Balogh et al. 1998; Baldry et al. 2004; Kauffmann et al. 2004; Blanton et al. 2005; Poggianti et al. 2008; Vulcani et al. 2010; Wetzel et al. 2012, see also Blanton & Moustakas 2009 for a review). It is also acknowledged that the fraction of blue star-forming galaxies increases in clusters with increasing redshift (so-called Butcher–Oemler effect, Butcher & Oemler 1978, 1984). These observations are the result of the gas supply that fuels the galaxy, and its consumption or removal (e.g., via feedback and/or stripping). These are functions of the environment (defined by galaxy number density or the distance to the fifth member, for example, to trace the dark-matter halo) for which complex hydrodynamical mechanisms of baryons and gravitational forces of dark matter are working behind.

Typical star-forming galaxies are generally defined on the plane of SFR–$M_\star$, and the normalization factor, the specific star-formation rate (sSFR) of such star-forming galaxies, evolves as a function of redshift (e.g., Daddi et al. 2007; Noeske et al. 2007; Whitaker et al. 2012; Speagle et al. 2014; Kurczynski et al. 2016) and increases with redshift at least up to $z \sim 6$ with fairly tight scatter (~0.3 dex). Therefore, more stars are formed in galaxies at higher redshift and at a given stellar mass. With the advent of large surveys revealing the gas content of star-forming galaxies, the evolution of sSFR appears to be caused by the higher gas fraction ($f_{\rm gas} = M_{\rm gas}/(M_{\rm gas} + M_\star)$), rather than a higher efficiency of transformation of gas into a

star, at least on the main sequence. Furthermore, the higher $M_{\rm gas}$ appears to mimic the higher gas supply rate (e.g., Magdis et al. 2012; Saintonge et al. 2013; Tacconi et al. 2013; Sargent et al. 2014; Genzel et al. 2015, hereafter G15; Scoville et al. 2014, 2016, hereafter S16, 2017; Schinnerer et al. 2016).

Since galaxies evolve not only as a function of redshift but also of their environment, one needs to understand how the gas content and its fraction changes with the environment, from fields to groups to clusters across cosmic time (where sSFR also evolves). With such understanding, we can determine whether star-forming processes are different or similar, e.g., in terms of global star-forming efficiency (SFE) or depletion timescale $\tau_{\rm depl.} = 1/{\rm SFE}$. This allows us to understand the physical mechanism driving galaxy evolution in different environments. Information on the gas content and its fraction is insufficient from environmental perspectives, specifically for high-redshift ($z \gtrsim 2$) clusters and their ancestors, i.e., proto-clusters. At $z = 0$, there is a large number of not only HI but also CO gas (to probe H_2) surveys (e.g., Boselli et al. 2014; Cybulski et al. 2016). Although the number of observations of clusters, groups, and voids is increasing, it is still limited; we are now beginning to understand how gas content changes as a function of environment at a fixed redshift (e.g., Chamaraux et al. 1980; Leon et al. 1998; Cortese et al. 2008; Chung et al. 2009; Serra et al. 2012; Boselli et al. 2014; Alatalo et al. 2015; Das et al. 2015; Mok et al. 2016).

Direct measurements of gas content of high-z (proto)cluster members are still limited to one or two samples of starbursts[19] (i.e., well above the main sequence >0.6 dex; e.g., Riechers et al. 2010; Tadaki et al. 2014) and AGNs (e.g., Emonts et al. 2013) per system. These rare populations are known to be more abundant in high-z overdensities than in general fields at the same redshift (e.g., Lehmer et al. 2013; Umehata et al. 2015; Casey 2016 and references therein). They are relatively easy to detect given their extreme nature (i.e., high SFR, brightness and/or richness of dust (submillimeter bright)). While the existence of these populations within high-z overdensities may play a profound role in galaxy evolution during the cluster-formation epoch, it is necessary to constrain the properties of typical (i.e., on the main sequence) star-forming galaxies to fully construct the picture of galaxy evolution, since they are a dominant population. There is no significant direct detection of molecular lines or dust continuum of the main-sequence galaxies in protoclusters (e.g., Hodge et al. 2013, but see Chapman et al. 2015 and references therein for a report of the detection of a normal (UV-faint) galaxy on the main sequence, with possibly CO (3–2) line emission), even though main-sequence star-forming galaxies have been reported to be dustier in a high-z (proto)cluster (e.g., Koyama et al. 2013).

In this paper, we reveal for the first time the gas content and its fraction of star-forming galaxies that are securely associated with a protocluster at $z = 2.49$, where multi-band ancillary data sets are available, as a case study. The term gas hereafter refers to the molecular gas as the measurement is, but it can be regarded effectively as the total gas mass at the considered resolution (∼a few kpc) because the atomic gas content might be negligible (within the effective radius) with higher ISM pressure at high redshift, particularly at the massive end (e.g., Obreschkow & Rawlings 2009; Lagos et al. 2012).

This is the first paper in a series of papers that will unveil the properties of star-forming galaxies associated with the proto-cluster 4C23.56 at $z = 2.49$. In this paper, we directly observe both gas, i.e., CO (3–2), and dust, meaning that we derive gas content without using an SFR-based empirical relation such as the Kennicutt–Schmidt (KS) relation (e.g., Schmidt 1959; Kennicutt 1998). This allows us to overcome uncertainties included in the conversion from SFR to gas mass and to check the consistency between two different measurements. Currently scheduled subsequent papers will report (1) the kinematics and structural properties of the galaxies combined with higher-resolution imaging (M. Lee et al. 2017, in preparation) and (2) UV-to-radio SED fitting and AGN contribution by adding X-ray (*Chandra*), mid-infrared (from IRAC and MIPS), and radio (Jansky Very Large Array; JVLA) data sets (M. Lee et al. 2017, in preparation).

The remainder of this paper is organized as follows. We illustrate the sample selection and introduce our target field in Section 2. In Section 3, we present details of the observations, data reduction, imaging, and analysis of the ALMA data. Section 4 presents a brief summary of ancillary data sets that are discussed within the paper. In Section 5, we present the measurements of barynoic gas mass and its fraction. We finally discuss the results by focusing on the different and similar properties found in the protocluster star-forming galaxies in Section 6. A summary is given in Section 7.

Throughout this paper, we assume $H_0 = 67.8$ km s^{-1} Mpc^{-1}, $\Omega_0 = 0.308$, and $\Omega_\Lambda = 0.692$ (Planck Collaboration et al. 2015). The adopted initial mass fuction (IMF) is Chabrier IMF in the mass range of 0.1–100 $M_\odot$.

2. Sample Selection and Target Field

2.1. Hα Emitters

We targeted Hα emitters (HAEs) that were originally detected using the narrow-band (NB) technique (Tanaka et al. 2011, I. Tanaka et al. 2017, in preparation) with MOIRCS/*Subaru* (Ichikawa et al. 2006). In the parent sample, 25 HAEs were detected within the field of view (FoV; ∼28 arcmin^2, corresponding to ∼84 comoving Mpc^2) of MOIRCS/*Subaru*. They are most likely associated with protocluster 4C23.56, given the width of the NB filter, which is $\Delta\lambda = 0.023$ μm with a central wavelength of 2.288 μm so that the Hα emission can be traced within $2.469 < z < 2.503$ (∼40 comoving Mpc). The redshift range corresponds to the velocity width of ±1500 km s^{-1}, which is sufficiently large to trace the non-virialized protocluster members. For reference, the velocity dispersion of Lyman alpha emitters (LAEs) associated to protoclusters at $z = 2$–3 is ∼200–1000 km s^{-1} (Venemans et al. 2007; Chiang et al. 2015). From simulations, the expected size of high-z protoclusters near $z = 2$–3 is $R_e \sim 5$–10 comoving Mpc depending on the size at $z = 0$ (Chiang et al. 2013; Muldrew et al. 2015).

The HAEs in the parent sample span three orders of magnitude in $M_\star$ and two orders of magnitude in SFR (Figure 1, I. Tanaka et al. 2017, in preparation; $0.2 <$ sSFR (Gyr^{-1}) < 301.0, and the typical sSFR of the main sequence is ∼1–3 (Gyr^{-1}; e.g.,

[19] We hereafter use the term "starburst" to refer to a galaxy well above the main sequence (>0.6 dex), which may include classical submillimeter bright (i.e., $S_{850\,\mu{\rm m}} > 5$ mJy) galaxies (SMGs). To be clear, SMGs refer to galaxies generally detected with a submillimeter single dish previously, which are thus unresolved and are a subpopulation of starbursts within this paper. We explicitly use the term "main-sequence SMGs" when these galaxies are, once resolved, on the main sequence (with smaller flux densities). This is to follow recent higher-resolution follow-up observations with ALMA demonstrating that such classical SMGs are divided into subgroups of starbursts and the main sequence when they are resolved (da Cunha et al. 2015).

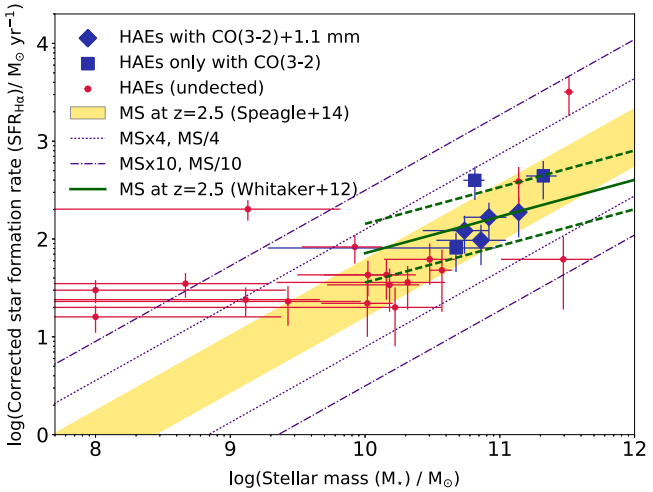

Figure 1. Distribution of galaxies in the SFR–$M_\star$ plane of the parent samples of HAEs (I. Tanaka et al. 2017, in preparation). The stellar mass is derived from the J and Ks bands and SFR is derived from the (continuum-subtracted) NB flux by considering dust extinction and [N II] contribution (see also Section 4.1 for a short description). We also plot lines for galaxies above ($\times 4$, $\times 10$, dotted) and below ($1/4$, $1/10$, dashed-dotted lines) the main sequence at $z = 2.5$. We used formulae presented in Speagle et al. (2014; yellow band) and Whitaker et al. (2012; green solid line and dashed lines for ± 0.3 dex) to show the $z \sim 2.5$ main-sequence galaxies. Most HAEs with stellar mass of $M\star > 10^{10}\ M_\odot$ are on the main sequence within the scatter of the main-sequence galaxies (± 0.3 dex), which will be the main targets discussed in this paper.

Whitaker et al. 2012; Speagle et al. 2014). In particular, the massive ($\gtrsim 10^{10}\ M_\odot$) galaxies mainly discussed in this paper are mostly on the main sequence. As such, the (NB-selected) HAEs have been studied to investigate the nature of typical (massive) star-forming galaxies on the main sequence (e.g., Geach et al. 2008; Sobral et al. 2009; Koyama et al. 2013; Tadaki et al. 2013; Oteo et al. 2015).

We observed the HAEs with the Atacama Large Millimeter/submillimeter Array (ALMA). The Band 3 CO (3–2) observations have been performed to cover 22 HAEs, and the Band 6 1.1 mm observations have been performed to cover 19 HAEs (See Figure 2). The targeted and detected numbers, while limited to the field coverage, constitute the largest sample of typical star-forming galaxies on the the main sequence associated with the protocluster that are probed for emission-line and dust-continuum observations. We have listed ALMA-targeted samples in Tables 1 and 2. The IDs in the first column are revised versions of those in Tanaka et al. (2011), and the reference IDs from Tanaka et al. (2011) are shown in the last column.

2.2. Protocluster 4C23.56

Protocluster 4C23.56 was identified as an overdense region of the NB-selected HAEs that was a part of the MAHALO-*Subaru* (MApping HAlpha and Lines of Oxygen with *Subaru*) survey (Kodama et al. 2015). Radio galaxy 4C23.56 (HAE1) at $z = 2.483 \pm 0.003$ is associated with this protocluster (Roettgering et al. 1997). Historically, radio galaxies have been targeted in a search for (proto)clusters since their hosts are the most massive galaxies (Seymour et al. 2007) and are expected to be embedded in the most massive halos (e.g., Rocca-Volmerange et al. 2004; Orsi et al. 2016). Indeed, the method has successfully yielded promising results to find (proto)clusters (e.g., Le Fevre et al. 1996; Kurk et al. 2000; Best et al. 2003; De Breuck et al. 2004; Overzier et al. 2006; Venemans et al. 2007; Hatch et al. 2011) and protocluster 4C23.56 is also one of them.

Protocluster 4C23.56 is known to have overdensities of differently selected galaxy populations besides HAEs (Tanaka et al. 2011). In other words, the protocluster is rich in ancillary data that ranges from X-ray to radio; therefore, it is one of the best targets to study the properties of typical star-forming galaxies in protocluster regions. Currently, the protocluster has been known to have (projected) overdensities of, for example, mass-selected distant red galaxies (DRGs) (Kajisawa et al. 2006), extremely red objects (EROs; Knopp & Chambers 1997), IRAC (Mayo et al. 2012), MIPS (Galametz et al. 2012) sources, and SMGs observed at 1.1 mm with the Atacama Submillimeter Experiment (ASTE; K. Suzuki 2013 PhD thesis; M. Zeballos et al. 2017, in preparation). These populations, however, have only rough (e.g., lower limit) or no redshift constraints compared to the relatively secure narrow redshift range of HAEs from the NB technique.

Nonetheless, some populations have several indirect evidences that imply an association with the protocluster. For example, three SMGs discovered with ASTE overlap the position of all of our HAEs except for HAE5, 11, 24, and 25 (Figure 3). The positions of three SMGs are also roughly coincident with the peak overdensity of the HAEs (with a resolution of $\sim 30''$). This has prompted the idea that HAEs associated to the protocluster are experiencing a dusty star-forming phase and the SMGs are associated with the protocluster. We followed up the HAEs (and the SMGs with overlaps) with ALMA, which allows us to pin down the 1.1 mm continuum.

3. ALMA Observations and Analysis

3.1. CO (3–2) at Band 3 and 1.1 mm at Band 6

ALMA 1.1 mm observations were performed in Cycle 1 and CO (3–2) observations were performed in Cycle 2 (ALMA# 2012.1.00242.S, PI: K. Suzuki).

The Band 6 continuum observations at 1.1 mm were conducted with a total on-source time of ~ 30 mins for eight-pointing target observations (typically ~ 4 mins per pointing direction), covering 19 out of 25 HAEs (Figure 2). The correlator is set to target four spectral windows with an effective bandwidth of ~ 1.875 GHz each that is taken in the time division mode (TDM; channel widths of 15.6 MHz or ~ 18 km s^{-1}). The central frequencies of the four spectral windows are 256.0, 258.0, 272.0, and 273.8 GHz. The noise level (1σ) reached ~ 0.08 mJy beam^{-1} per field, except for one case with ~ 0.12 mJy beam^{-1} where a bright SMG 4C23 AzTEC1 SMG ($S_{1.1\ \mathrm{mm,single\ dish}} = 10$ mJy) is located (K. Suzuki 2013 PhD thesis; M. Zeballos et al. 2017, in preparation). The baseline lengths were between 17 and 462 m. We observed J2148+0657, Neptune, and J2025+3343 as a bandpass, flux, and phase calibrator, respectively.

The Band 3 CO(3–2) observations were executed for a total of 4 hr of on-source time with four-pointing (thus ~ 1 hr per pointing direction), targeting 22 HAEs. The correlator is set to target four spectral windows with effective bandwidth of ~ 1.875 GHz each. One of the spectral windows, centered at 99.3 GHz, is taken in frequency division mode (FDM; channel widths of 0.49 MHz or ~ 1.5 km s^{-1}), where the redshifted

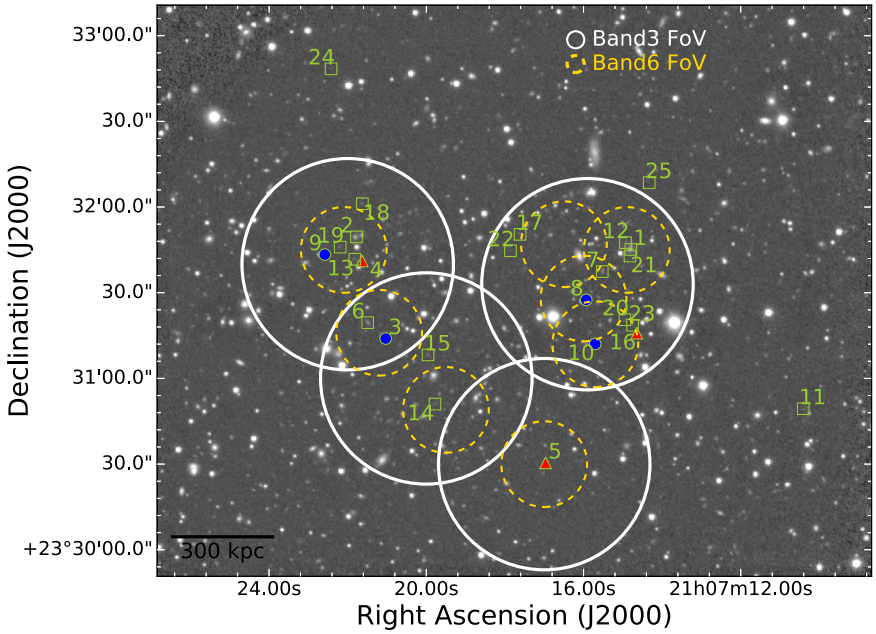

Figure 2. Distribution of HAEs tagged by the source ID, overlaid on the *Subaru*/MOIRCS Ks-band image (I. Tanaka et al. 2017, in preparation). The blue filled circles indicate galaxies detected simulataneously in CO (3–2) and 1.1 mm, red triangles indicate galaxies only in CO (3–2). Green open squares show the remainder of HAEs detected with the NB filter technique. The fields of view (FoVs) of ALMA Band 3 CO (3–2) (white open circles) and Band 6 1.1 mm (yellow dashed circles) observations are shown on the map. The total number of pointing is 4 and 8 for Band 3 and Band 6, respectively. A scale bar is shown at the bottom left corner to represent the physical size of 300 kpc.

CO(3–2) line ($\nu_{\rm rest}$ = 345.79599 GHz) at $z = 2.5$ would fall, while the remaining three spectral windows are taken in the TDM mode (a channel width of 15.6 MHz or 47 km s^{-1}) and are centered at 101.1, 111.3, and 113.2 GHz. The velocity coverage of the CO observations is ∼6400 km s^{-1}, corresponding to a redshift coverage of $2.385 < z < 2.516$ in the lower side band and $2.031 < z < 2.134$ in the upper side band. This is sufficient to cover the expected redshift range of the 22 HAEs detected by the NB technique ($z = 2.486 \pm 0.017$). All 19 HAEs covered by the 1.1 mm observations were fully covered by the Band 3 observations (Figure 2). The typical noise (1σ) level reached ∼0.17 mJy when the spectral resolution is re-binned to 100 km s^{-1}. We chose a spectral resolution of 100 km s^{-1} to estimate the signal-to-noise ratio (S/N; as the detection criteria, see Section 3.2.1) and upper limits for non-detection, except for a case in which we needed a higher velocity resolution. For example, the treatment was applied for HAE5 since we found strong emission in a single channel with S/N > 6.5. Thus, we re-imaged the source with a spectral resolution of 30 km s^{-1} and found that the fitted line width is FWHM ∼ 100 km s^{-1}. The noise level in this case became worse, i.e.,∼0.3 mJy, but it was sufficient in that the detection of this galaxy satisfied our detection criteria (see Section 3.2.1). The flux calibrator was Titan for Band 3. J1751 +0939 and J2148+0657 were chosen as bandpass calibrators and J2025 + 3343 as a phase calibrator. The minimum baseline was 43 m, and the maximum baseline was 1574 m for Band 3.

We applied the CLEAN algorithm to the calibrated visibilities with natural weighting to produce images for both observations by using the Common Astronomy Software Applications package (CASA, used 4.2.2 version for calibration and imaged with 4.6.0 version). The absolute flux uncertainties for both bands were estimated as ∼15%–18%, which were not taken into account for the flux error throughout this paper. The synthesized beam sizes are $0\farcs91 \times 0\farcs66$ (PA = 23.°5) for Band 3 and $0\farcs78 \times 0\farcs68$ (PA = 0.°4) for Band 6. The sub-arcsec resolution is sufficient to pin down SMGs detected by ASTE (with its typical beam size of ∼30″) and to search for counterparts detected at other wavelengths, e.g., images obtained in NIR/optical bands.

3.2. Detection and Flux Measurement

3.2.1. Detection Criteria

We searched for emissions around the position of HAEs with a searching radius of $r = 1''$. We regarded a galaxy as detected in ALMA Band 6 (1.1 mm continuum) if a peak flux density is above 4σ. A CO (3–2) line was regarded as detected if at least two among three criteria (a)–(c) were satisfied: (a) a peak flux $>4\sigma$, (b) at least two continuous channels including a maximum peak flux channel have flux $>3.5\sigma$, and (c) (spatially smoothed) velocity-integrated peak fluxS/N is above 5 before the primary-beam correction. All galaxies except HAE4 (=6/7) satisfy all the conditions. HAE4 has two distinct but not continuous peaks ($>4\sigma$) that are 100 km s^{-1} (one channel) apart (Figure 4). We show CO (3–2) spectra in Figures 4–7, but a detailed analysis that deals with the kinematics and sizes is beyond the scope of this paper and will be presented in a subsequent paper (M. Lee et al. 2017, in preparation).

We note that the detection is not a false identification of spurious or other lines at a different redshift, provided the redshift range of the NB filter and our on-going parallel NIR spectroscopy using the upgraded MOIRCS ("nuMOIRCS") on board *Subaru*. The spectroscopic campaign has thus far confirmed the redshifts of 15 HAEs that are all within $z = 2.49 \pm 0.01$ (I. Tanaka et al. 2017, in preparation). We defined the CO (3–2) redshift from the median velocity component due to the broad nature of the spectrum for many of the galaxies. The CO redshift is consistent with the NIR spec-z value within an error of

Table 1
Source Information for Detection

Source ID	R.A.$_{CO32}$ (J2000)	Decl.$_{CO32}$ (J2000)	$M_\star$ $\times 10^{10}\ M_\odot$	SFR$_{H\alpha,corr}$ $M_\odot\ yr^{-1}$	$z_{CO\,(3-2)}$	$I_{CO\,(3-2)}$ Jy km s^{-1}	line width km s^{-1}	$S_{1.1\ mm}$ mJy	$M_{gas,CO32}$ $\times 10^{10}\ M_\odot$	$M_{gas,dust}$ $\times 10^{10}\ M_\odot$	SFE Gyr^{-1}	$f_{gas,CO}$	ID in T11
HAE3	316.837650	23.520500	13.0 ± 1.9	176 ± 78	2.4861	0.352 ± 0.06	500	0.53 ± 0.14	10.55 ± 1.8	5.9 ± 2.16	1.68	0.45	354
HAE4	316.840213	23.527986	19.7 ± 5.1	414 ± 175	2.478	0.246 ± 0.03	300	<0.54	6.86 ± 0.84	<6.22	6.04	0.26	479
HAE5	316.820742	23.508458	6.1 ± 1.1	374 ± 140	2.4873	0.09 ± 0.02	100	<0.33	3.14 ± 0.7	<3.96	11.95	0.34	153
HAE8	316.816433	23.524292	7.8 ± 2.7	156 ± 63	2.4861	0.263 ± 0.03	300	0.75 ± 0.12	8.69 ± 0.99	8.35 ± 2.51	1.81	0.53	431
HAE9	316.844121	23.528694	6.8 ± 3.6	90 ± 40	2.4861	0.542 ± 0.06	1000	1.21 ± 0.21	18.43 ± 2.04	13.48 ± 4.14	0.49	0.73	511
HAE10	316.815525	23.520000	5.1 ± 2.6	115 ± 47	2.4861	0.362 ± 0.06	500	0.44 ± 0.12	13.15 ± 2.18	4.9 ± 1.83	0.88	0.72	356
HAE16	316.811025	23.520958	4.4 ± 4.3	76 ± 32	2.4826	0.493 ± 0.07	600	<1.1	18.52 ± 2.63	<12.5	0.41	0.81	···

Table 2
Information for Undetected Sources

Source ID	R.A.$_{\rm H\alpha}$ (J2000)	Decl.$_{\rm H\alpha}$ (J2000)	$S_{\rm CO32}$[a] mJy	$S_{1.1\ \rm mm}$ mJy	$M_{\rm gas,CO32}$ $\times 10^{10}\ M_\odot$	$M_{\rm gas,dust}$ $\times 10^{10}\ M_\odot$	ID in T11
HAE1	316.811658	23.529211	<0.67	<0.32	<11.07	<3.54	491
HAE2	316.840738	23.530434	<0.52	<0.50	<8.61	<5.60	526
HAE6	316.839548	23.522090	<0.95	<0.46	<15.66	<5.08	393
HAE7	316.814680	23.527065	<0.52	<0.86	<8.52	<9.56	⋯
HAE12	316.812222	23.529876	<0.67	<0.32	<11.12	<3.56	⋯
HAE13	316.840917	23.528263	<0.49	<0.43	<8.02	<4.79	500
HAE14	316.832414	23.514173	<0.53	<0.70	<8.68	<7.79	⋯
HAE15	316.833151	23.518959	<0.52	⋯[b]	<8.56	⋯[b]	⋯
HAE17	316.823395	23.530683	<1.02	<1.07	<16.92	<11.93	543
HAE18	316.840110	23.533663	<0.7	⋯[b]	<11.54	⋯[b]	⋯
HAE19	316.842465	23.529443	<0.5	<0.37	<8.21	<4.12	⋯
HAE20	316.812277	23.522381	<0.65	<1.01	<10.67	<11.20	⋯
HAE21	316.811748	23.528571	<0.63	<0.33	<10.45	<3.67	⋯
HAE22	316.824409	23.529090	<1.03	⋯[b]	<17.09	⋯[b]	⋯
HAE23	316.811469	23.521843	<0.71	<1.10	<11.71	<12.27	⋯

Notes.
[a] At 100 km s^{-1} resolution per channel. 3σ upper limit.
[b] ALMA 1.1 mm observation has no coverage.

$\Delta z = 0.004$ for most of the cases, but $\Delta z = 0.01$ for HAE3 and HAE4 owing to the low S/N in the NIR spectroscopy.

3.2.2. Flux

We adopted a peak flux at 1.1 mm or a peak velocity-integrated flux in the CO (3–2) moment 0 map to compute gas mass, which was measured from a smoothed map. We measured the flux after primary-beam correction. All of the sources are within a good sensitivity region; thus, the measured flux was not changed significantly by the primary-beam correction (within ∼10%). The noise level for the flux uncertainty in Band 3 was estimated by averaging five line-free channels in the primary-beam-corrected image, which was cut out around the source (with a size of $15 \times 15''$) using `immath` from the original map with FoV of $\sim 74''$ and then masked (with a radius of 1.5 times the beam size) for the known bright sources (including HAEs). Similarly, the noise level in Band 6 was derived from the image sliced around the source with a size of $6'' \times 6''$ from a larger image with FoV $\sim 30''$ and then masked for the detected known sources.

We smoothed images using the CASA command `imsmooth`. This treatment was performed to neglect a galaxy structure for the measurement of global gas content. We found that image-based smoothing delivers a better S/N than tapering the uv visibilities. In addition, smoothing allows us to avoid the divergence of 1-component Gaussian spectrum fitting for a disturbed galaxy, which likely constitutes roughly half of the detected HAEs. The images in Band 3 for CO (3–2) were smoothed channel by channel. By making a measurement from the smoothed map, we could also maximize the S/N by collecting diffuse, extended emissions from the outskirts of a galaxy that could be missed with the sub-arcsec (∼6 kpc at $z = 2.5$) beam size.

We adopted a smoothing Gaussian kernel size of $0\farcs8 \times 0\farcs8$ for Band 6 and $0\farcs6 \times 0\farcs6$ for Band 3. A detailed analysis of the choice of Gaussian kernels is presented in Appendix A. In brief, we investigated S/N as a function of the smoothing kernel, which is effectively equivalent to considering the growth curve of galaxy emission as a function of aperture size. This results in a similar smoothed beam size of $1\farcs1 \times 0\farcs9$ for Band 3 and $1\farcs1 \times 1\farcs0$ for Band 6. We find that, at the adopted beam sizes, the S/N is maximum and the flux is ∼50%–90% of the maximum flux measured up to $4\farcs0$ (physical size of ∼33 kpc at $z = 2.5$) smoothing kernel. We show the growth curves as a function of the smoothing Gaussain kernel in Figures 14 and 15 to show that the adopted kernel is not a bad choice. We note that some galaxies have a low recovery flux with respect to the maximum peak value, but all these have a relatively low S/N; therefore, the uncertainty is also large in the absolute flux. Thus, we opt to choose the universal smoothing kernels for the analysis. The beam sizes correspond to ∼8.5 kpc in physical scale for both 1.1 mm and CO (3–2) and are sufficient to recover the total flux given the typical size of a star-forming galaxy at high z ($r_{1/2,\rm CO} \sim 5$ kpc, e.g., Bolatto et al. 2015).

Instead of performing a Gaussian fit for CO (3–2), we compute and choose an integrating range for CO (3–2) to obtained the maximum S/N in the peak flux in the velocity-integrated image following the description in Seko et al. (2016). The map was checked by eye afterward for unexpected cases, such as extremely broad-line widths to integrate, because some galaxies have unusual spectra that are not well-fitted with a single Gaussian, in addition to inhomogeneous spatial distributions and the velocity gradients (see Figures 4–7 for the morphology and spectrum, M. Lee et al. 2017, in preparation).

With our detection criteria, we detect seven and four HAEs in CO (3–2) and dust continuum out of 22 and 19 HAEs, respectively, in our targeted fields (see also Figures 4–7 for a gallery of detected sources). We summarize flux values for detected sources in Table 1, and for non-detection in Table 2. The detected sources have stellar mass $>4 \times 10^{10}\ M_\odot$, and two of them have stellar masses exceeding $\sim 10^{11}\ M_\odot$ (HAE3, HAE4).

4. Ancillary Data

4.1. MOIRCS/Subaru NIR Data: Mstar and SFR

The stellar masses ($M_\star$) and SFRs of the HAEs are derived from the broadband emissions in J and Ks bands and the Hα

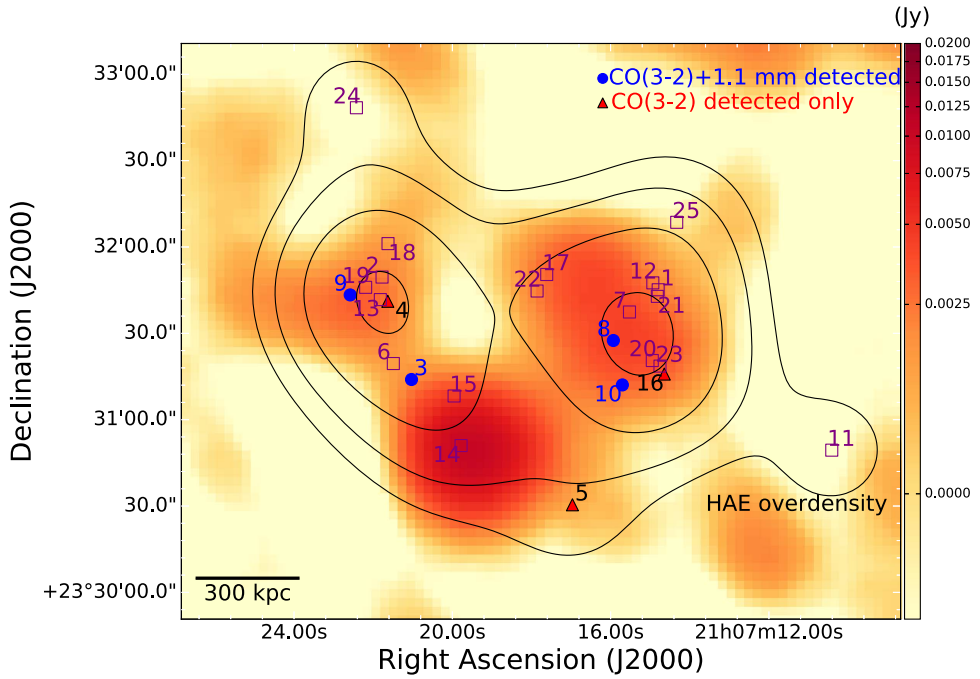

Figure 3. Distribution of HAEs tagged by the source ID, overlaid on the AzTEC/ASTE 1.1 mm single dish image (background color, K. Suzuki 2013 PhD thesis; M. Zeballos et al. 2017, in preparation). Multiple SMGs are nicely overlapped with HAEs, suggesting that HAEs are undergoing a dusty star formation. The brightest SMG (4C23-AzTEC 1) detected with AzTEC/ASTE at 1.1 mm, near HAE14, is not associated with the protocluster (K. Suzuki et al. 2017, in preparation). Thus, relatively moderate star-forming galaxies on the main sequence appear to be associated with the protocluster. Four blue filled circles are for galaxies detected simultaneously in CO (3–2) and 1.1 mm, red triangles for the CO (3–2) only detection, and purple squares for the rest of the HAEs. The ALMA observations have confirmed the association of 1.1 mm dust-continuum emission for four HAEs (HAE3, 8, 9, 10). The number next to the color bar on the right is written in the unit of Jy to show the flux level of the 1.1 mm AzTEC sources. We also plot an HAE surface overdensity map in black contours that is estimated by assuming a Gaussian kernel with a radius of 0.′ 8 that corresponds to the physical size of 400 kpc in radius (or ∼1.4 comoving Mpc in radius), in steps of [1, 2, 4, 8] (arbitrary unit; Section 6.5.1).

emissions within the NB filter, respectively. The observations are executed under the seeing-limited condition, i.e., 0.″7. Thus far, we have obtained eight broad/intermediate/narrow-band images in the optical-to-near-infrared (NIR) range by using *Subaru*, i.e., *B*, IA427, r', z', *J*, *H*, *Ks*, and NB2288 (which is called the "CO"-filter). However, we chose to use only the above three bands because the data quality (i.e., the depth and resolution) is not as good as that in longer-wavelength imaging (I. Tanaka et al. 2017, in preparation). Further analysis to deal with such data combining data at longer wavelengths up to radio wavelengths will be presented in one of the following papers.

Since the full description of the data reduction and analysis for these observations will be presented in I. Tanaka et al. 2017, (in preparation), we present here only a brief summary of the derivation of physical parameters that are used throughout this paper. The stellar mass is derived using $[J-Ks]$ color and *Ks* magnitude and calibrated from empirical fitting between Bruzual & Charlot (2003; BC03) and the spectral energy distribution (SED) fitting with the FAST code.[20] The star-formation rate (SFR) is converted using the method described in Kennicutt & Evans (2012) from the Hα flux that is measured from the NB filter excess. The intrinsic star-formation rate is estimated by taking into account dust extinction in the Hα emission using the method described in Garn & Best (2010), which employs mass-dependent extinction correction. This correction method appears to hold up to $z \sim 1.5$ (Sobral et al. 2012; Domínguez et al. 2013; Ibar et al. 2013) and is often used for distant galaxies ($z \sim 2$) as a proxy for dust extinction (e.g., Sobral et al. 2014). We will discuss the effect of the adopted dust correction method in Section 6.2.

For massive galaxies ($M_\star > 10^{10}\ M_\odot$), the HAEs are, in general, located near the main sequence defined at $z = 2.5$ (Whitaker et al. 2012; Speagle et al. 2014) in Figure 1. We also plot two SFR–$M_\star$ relations to follow a few studies claiming the nonlinearity of the relation (e.g., Whitaker et al. 2012, 2014; Lee et al. 2015). In this case, the slope of the star-forming sequence is flattened at the high-mass end. However, even if we take this effect into account (green dashed lines in Figure 1), the most massive HAEs are still within a scatter of the main sequence (∼0.3 dex). The outliers on the massive end are (potential) AGNs such as HAE1 (which is the radio galaxy 4C23.56) and HAE5 (Tanaka et al. 2011), the $\mathrm{SFR_{H\alpha}}$ values of which are probably overestimated owing to AGN contamination, or HAE7, which is undetected in both CO (3–2) and 1.1 mm, expectedly have a low gas budget at the given stellar mass, and might be close to quenching or becoming passive.

Low-mass galaxies have large uncertainties in stellar masses, mainly because of large errors in photometry of both the Ks and J bands with a low S/N. We tentatively found a signature of enhanced star formation at a given stellar mass that is similarly observed in other protocluster members (Hayashi et al. 2016; I. Tanaka et al. 2017, in preparation). While the SFRs might be overestimated for the less massive galaxies (e.g., see Figure 8 in Shivaei et al. 2016), further investigation is beyond the scope of this paper. Since the galaxies detected in

[20] http://w.astro.berkeley.edu/~mariska/FAST.html

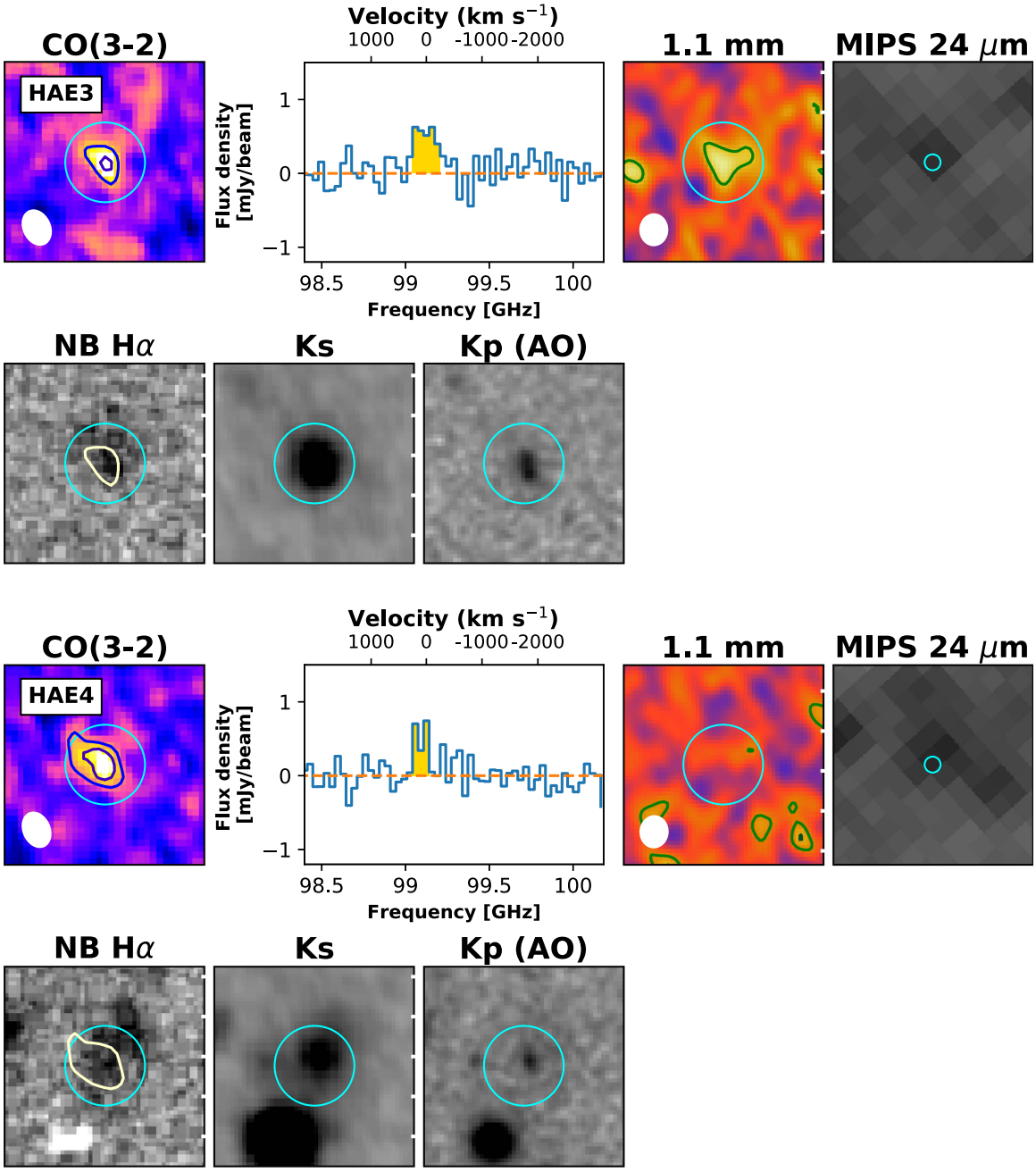

Figure 4. Multi-band images of sources detected using ALMA with either CO (3–2) or 1.1 mm detection for HAE3 (top two rows) and HAE4 (bottom two rows). From left to right (upper row of each target): CO (3–2) integrated intensity, CO (3–2) spectrum at the peak, 1.1 mm, MIPS 24 μm, (lower row; continuum-subtracted NB Hα, Ks, and Kp (AO). The center of each panel is set by the CO (3–2) peak position. We plot contours of CO (3–2) and 1.1 mm emission in steps of 2σ starting from 3σ since the color scales of the panels are slightly different. The beams of CO (3–2) ($0\farcs91 \times 0\farcs66$, PA $= 23\fdg5$) and 1.1 mm ($0\farcs78 \times 0\farcs68$, PA $= 0\fdg4$) are shown on the bottom left. The CO (3–2) spectrum is shown for the range between 98.4 and 100.2 GHz into which the redshifted CO(3–2) at $z \sim 2.5$ would fall. The velocity resolution is set to 100 km s^{-1} in general, but it is set to 30 km s^{-1} for HAE5 (see Figure 5). The yellow region of each spectrum is the integrating velocity range that delivers the highest S/N (Section 3.2.2). The 3σ for the CO (3–2) contour is also overlaid on each NB Hα image for comparing the distribution. In the AO images, we find compact components for the most massive galaxies among those detected (HAE3 and 4), while the restare is marginally visible, suggesting the relatively diffuse nature of the stellar component. We also plot a cyan circle with a radius of 1″, which is also centered on the peak position of CO(3–2), to show the scale of the panel and to point out that the counterpart at different wavelengths is located near the CO(3–2) position or within 2″ in general (see also Appendix B). Because the MIPS/Spitzer observations at 24 μm have a coarse resolution compared to those of other bands, we zoom out images to clearly show the detection.

the ALMA observations are massive enough, the uncertainties in less massive galaxies would not critically affect our discussion.

Additionally, we recently obtained adoptive optics (AO)-supported K' band images with IRCS/*Subaru* with a resolution of $0\farcs2$ for several HAEs where a natural guide star is available (Y. Koyama et al. 2017, in preparation; M. Lee et al. 2017, in preparation). The AO images are shown in Figures 4–7 to provide some visual hints for understanding the nature of the galaxies, but a full description and detailed analysis of the observation will be presented in the following subsequent papers.

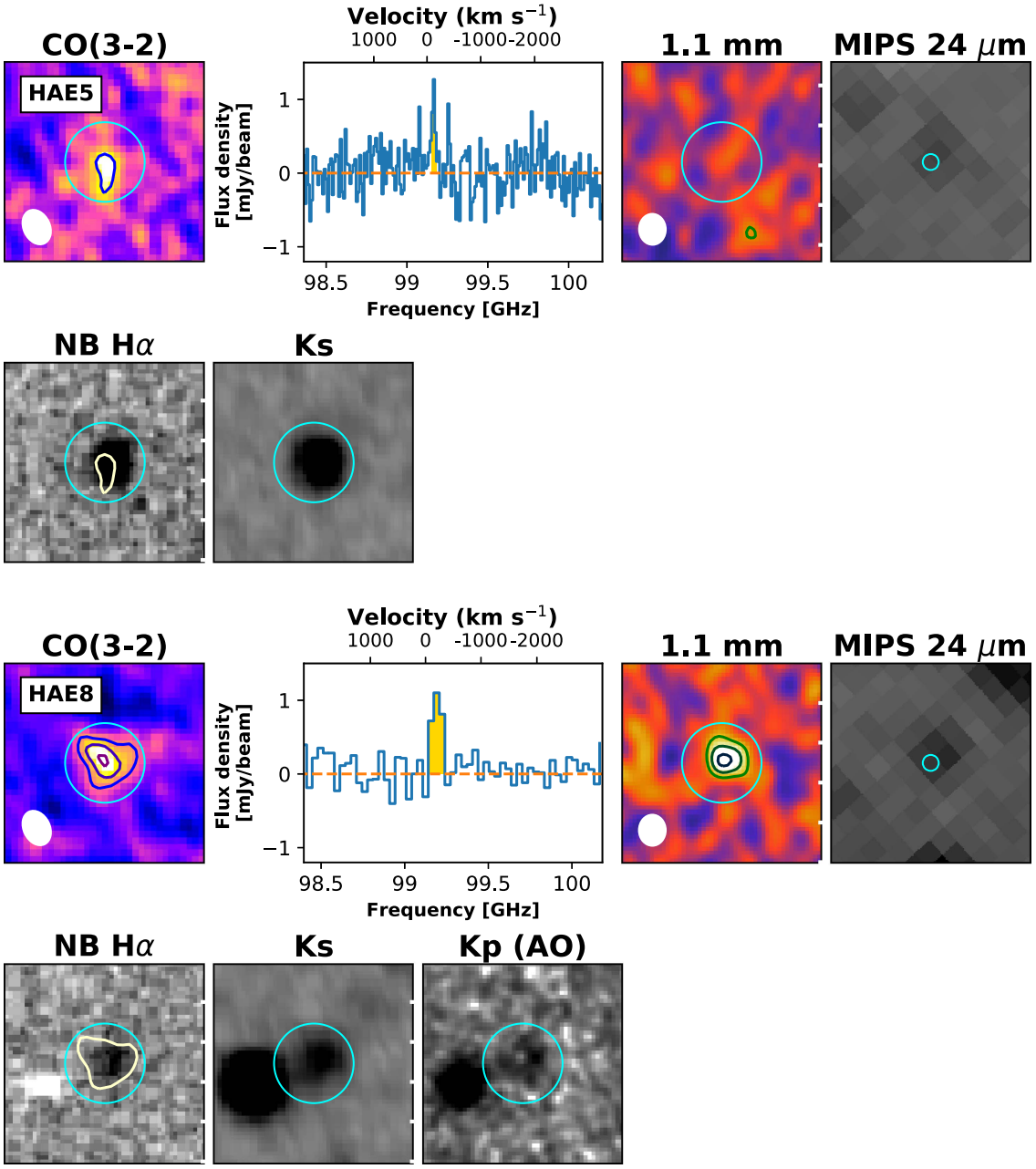

Figure 5. Multi-band images for the galaxies having either CO (3–2) or 1.1 mm detection (continued): HAE5 (top two rows) and HAE8 (bottom two rows). Refer to Figure 4 for the description of each panel and symbol. There was no coverage of the AO observation in Kp for HAE5. Since the line width for HAE5 is narrow (see also the text and Table 1), we show the spectrum with a velocity resolution of 30 km s^{-1}, as opposed to other galaxies, which are shown with a resolution of 100 km s^{-1}.

4.2. Spitzer: MIPS 24 um

We also utilized archival data sets of 4C23.56 (PI: A. Stockton; Program ID 30240) at 24 μm observed with MIPS/*Spitzer*, which were retrieved from the Spitzer Heritage Archive (SHA) interface.[21] We used MOPEX software package for image processing. We present the MIPS image only to show the visual characteristics (i.e., whether a detection occurred) of the HAEs with Band 3/6 detections (Figures 4–7).

5. Gas Mass

We measured the total gas mass from the estimated flux (Section 3.2.2) of dust continuum and CO (3–2) line emission. In the following two sections, we address how the gas mass is estimated.

5.1. CO (3–2) to Gas Mass

Although the CO line emission constitutes only a fraction of the total gas content, the strategy of using the optically thick CO line emission in the total gas mass was established around the time millimeter observations became available in the late 1980s (Dickman et al. 1986; Solomon et al. 1987). While higher-J rotational transitions of CO have large uncertainty for the unknown excitation, lower-J ($J < 4$) lines are a good probe for the total cold gas mass (e.g., Carilli & Walter 2013), and the lines have been used for several pioneering works on high-z

[21] http://sha.ipac.caltech.edu/applications/Spitzer/SHA/

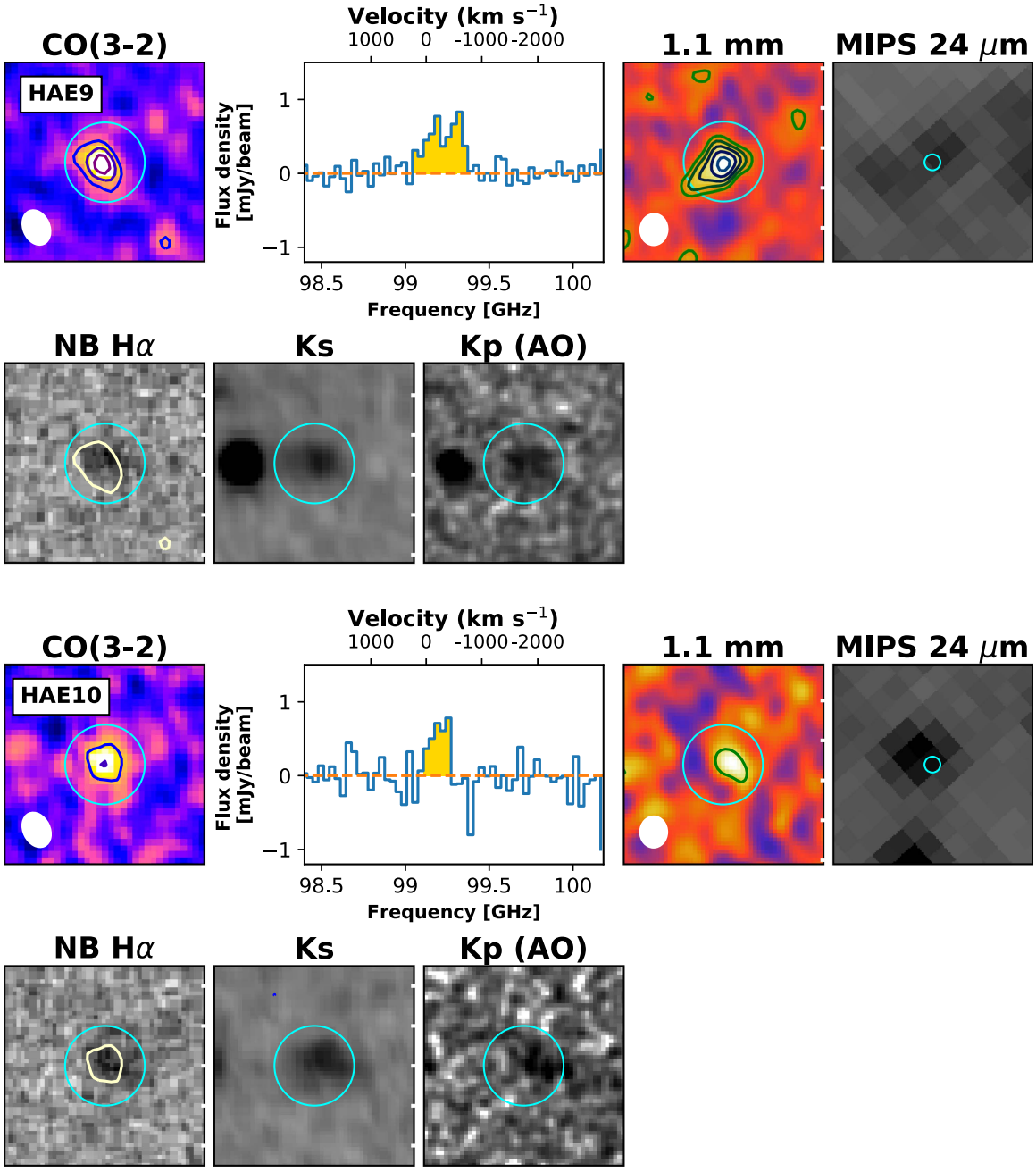

Figure 6. Multi-band for the galaxies having either CO (3–2) or 1.1 mm detection (continued): HAE9 (top two rows) and HAE10 (bottom two rows). Refer to Figure 4 for the description of each panel and symbol.

star-forming galaxies as well as SMGs (e.g., Magdis et al. 2012; Tacconi et al. 2013; Daddi et al. 2015)

We derived the gas mass from CO (3–2) emission by following the prescription presented in Genzel et al. (2015). Provided (massive) HAEs are on the main sequence, and a typical conversion factor for normal star-forming galaxies or Milky-way-like galaxies, $\alpha_{\rm MW} = 4.36\ M_{\odot}({\rm K\ km\ s^{-1}\ pc^2})^{-1}$, is adopted to the first order. Then the metallicity (Z) dependence of the conversion factor, i.e., $\alpha_{\rm CO\,1} = \alpha_{\rm MW} \times A(Z)$, is considered. $A(Z)$ corresponds to the metallicity dependence of the conversion factor calculated by taking the geometric mean of Bolatto et al. (2013) (the Equation (6) in G15) and Genzel et al. 2012 (the Equation (7) in G15).

To account for the metallicity dependence of the conversion factor, we adopted the galaxy's metallicity derived from an empirical mass–metallicity relation, as presented in Genzel et al. (2015; equation (12a), which uses a fitting function of Wuyts et al. 2014). The adopted metallicity-dependent conversion factor is in the range of $\alpha_{\rm CO,1} = [4.4, 5.9]$. The reason for using the empirical relation is that we still had incomplete metallicity measurements for all of the samples; only a fraction of [N II] and Hα spectroscopic data are obtained and some have low S/Ns. Within the stellar mass range of HAEs detected in CO (3–2) and dust-continuum ($4 \times 10^{10} < M_{\star}/M_{\odot} < 2 \times 10^{11}$), the metallicity varies within a modest range of ([8.50, 8.65]) even if we adopt a different metallicity recipe; for example, the one described in Mannucci et al. (2010) would yield a value lower by <0.02 dex, which results in a conversion factor that does not vary by more than a factor of 2. It is worth noting that there might be a

tendency of lower metallicity in the high-z overdense region (e.g., Valentino et al. 2015), where a pristine gas is likely being accreted from the cosmic web, particularly at high redshift. However, this is controversial given several contradictory cases, such as higher metallicity (e.g., Steidel et al. 2014; Shimakawa et al. 2015), a flat mass–metallicity relation (thus, higher metallicity in lower mass regime, e.g., Kulas et al. 2013), and the same mass–metallicity relation as fields (e.g., Tran et al. 2015) at $z \sim 2$. Therefore, we stick to the general comprehension of the stellar mass–metallicity relation. We discuss the validity of the choice of conversion factor in Section 6.3.

We use a standard luminosity (brightness temperature) line ratio between different rotational transitions of CO, i.e., CO (1–0)-to-CO(3–2) ratio $R_{13} = 1.9$, which can be applied to both high-z typical star-forming galaxies and SMGs (e.g., Tacconi et al. 2008, 2013; Carilli & Walter 2013; Daddi et al. 2015).

The gas mass is then computed as expressed by Equation (1) at a given luminosity $L'_{\mathrm{CO}\,J}$ by using a conversion factor $\alpha_{\mathrm{CO}\,1}$, CO $J \rightarrow J-1$ line flux $F_{\mathrm{CO}\,J}$, source luminosity distance D_L, redshift z, and observed line wavelength $\lambda_{\mathrm{obs}\,J} = \lambda_{\mathrm{rest}\,J}(1+z)$ (Solomon et al. 1997; Bolatto et al. 2013), where $J = 3$ in our case.

$$\begin{aligned} M_{\mathrm{gas,CO}}\,[M_\odot] &= \alpha_{\mathrm{CO}\,1} \times L'_{\mathrm{CO}\,1} \\ &= 1.57 \times 10^9 \left(\frac{\alpha_{\mathrm{CO}\,1}}{\alpha_{MW}} \times \frac{R_{1\,3}}{}\right) \\ &\quad \times \left(\frac{F_{CO\,3}}{\mathrm{Jy\ km\ s^{-1}}}\right) \times (1+z)^{-3} \\ &\quad \times \left(\frac{\lambda_{\mathrm{obs}\,3}}{\mathrm{mm}}\right)^2 \times \left(\frac{D_L}{\mathrm{Gpc}}\right)^2. \end{aligned} \tag{1}$$

Since we aim to compare our survey with other high-z field[22] surveys based on either CO and/or dust continuum, we apply the same analysis for the available data set.

For a CO-based survey, we referred to the PHIBBS-I sample presented in Tacconi et al. (2013).[23] The PHIBBS-I galaxies are located in several fields including the Great Observatories Origins Deep Survey-North (GOODS-N) field, Q1623, Q1700, Q2343, and Extended Groth Strip (EGS) field. This is a CO(3–2) survey of massive galaxies ($\log(M_\star/M_\odot) \geqslant 9.5$) scattered around the main-sequence star-forming galaxies between $1 < z < 3$. Later, we select PHIBBS-I galaxies within the main sequence (± 0.3 dex using Whitaker et al. 2012) at $2 < z < 3$ above $\log(M_\star/M_\odot) > 10.6$, which are unfortunately only seven in number, and its stellar mass range is $10.6 \leqslant \log(M(M_\star)) \leqslant 11.2$, which is almost the same stellar mass range as that detected in CO(3–2) (i.e., $10.6 \leqslant \log(M(M_\star)) \leqslant 11.3$). We apply the same gas recipe for the PHIBBS-I galaxies, while the values of $M_\star$ and SFR are simply adopted from Table 2 in Tacconi et al. (2013), which is derived from SED fitting.

[22] We assume that the compared galaxies are in "general" fields, which may have probed a presumably large volume (i.e., a relatively wide redshift range to cover thelarge-scale structure); thus, cosmic variance may not significantly affect the comparison.

[23] At the date of submission, the PHIBBS-2 sample was not yet available online (Tacconi et al. 2017).

We summarize the measured CO line flux and the derived total molecular gas masses for individual HAEs in Table 1. The derived molecular mass ranges between (0.3–1.9) $\times 10^{11}\ M_\odot$. The upper limit of molecular gas mass is set to 3 σ assuming a velocity width of $\sim$300 km s^{-1}, i.e., a typical galactic disk rotation, as presented in Table 2.

5.2. 1.1 mm Dust to Gas Mass

We derive gas mass from dust-continuum detection using a method presented in S16. As S16 and Berta et al. (2016) have argued, the dust mass fitted with the FIR-only SED (i.e., using an SED model that is fitted only around the FIR peak with Herschel) would yield significant uncertainties in measuring total gas mass, since the flux around the peak is no longer optically thin; therefore, the dust (and gas) mass fitted by the SED model is a rather luminosity-weighted value. Therefore, we assume a dust temperature of 25 K to weigh the global gas amount as suggested in Scoville et al. (2014), and S16. They derived the gas mass using the Rayleigh–Jeans (RJ) tail of the dust spectrum and by adopting a locally calibrated luminosity–mass relation. The gas mass is calculated as follows.

$$\begin{aligned} M_{\mathrm{gas,dust}}\,[M_\odot] &= \frac{1.78 \times 10^{10}}{(1+z)^{4.8}} \left(\frac{\Gamma_{\mathrm{RJ}}}{\Gamma_0}\right)^{-1} \frac{6.7 \times 10^{19}}{\alpha_{850}} \\ &\quad \times \left(\frac{S_\nu}{\mathrm{mJy}}\right)\left(\frac{\nu}{353\ \mathrm{GHz}}\right)^{-3.8}\left(\frac{D_\mathrm{L}}{\mathrm{Gpc}}\right)^2 \end{aligned} \tag{2}$$

where S_ν is the observed dust-continuum flux in mJy, α_{850} is a constant for calibrating luminosity to gas mass, and $\frac{\Gamma_{\mathrm{RJ}}}{\Gamma_0}$ is the RJ correction factor with $\Gamma_0 = \Gamma_{\mathrm{RJ}}(0, T_d, \nu_{850}) = 0.71$ and Γ_{RJ} given by

$$\Gamma_{\mathrm{RJ}}(T_d, \nu_{\mathrm{obs}}, z) = \frac{h\nu_{\mathrm{obs}}(1+z)/kT_d}{e^{h\nu_{\mathrm{obs}}(1+z)/kT_d} - 1}. \tag{3}$$

The metallicity dependence of the dust-based calibration may not affect our discussion since the stellar mass range of the detected sources are sufficiently large. However, we note that the dust-based measurement may yield a systematically lower value than the CO-based measurements (e.g., Genzel et al. 2015; Decarli et al. 2016b; see also some discussions in Section 6.3 and Figure 8).

The calculated results for 1.1 mm are also summarized in Table 1, and images are shown in Figures 4–7. We find that the gas mass derived from 1.1 mm is in the range of (0.5–1.4) $\times 10^{11}\ M_\odot$ for four objects.

Similarly, for CO (3–2), for the comparison with field galaxies, we referred to the study of S16, which targeted galaxies extensively in the Cosmic Evolution Survey (COSMOS) field within the redshift range of $1 < z < 6$. We also applied the same analysis for ALMA LABOCA Extended *Chandra* Deep Field-South Survey (ECDF-S) Submm Survey (ALESS) SMGs, which are partly covered in GOODS-S. We particularly focus on the main-sequence SMGs within a redshift range of $2 < z < 3$, the stellar mass of which is restricted to $\log(M_\star/M_\odot) > 10.6$; therefore, $10.4 \leqslant \log(M(M_\star)) \leqslant 11.7$. The gas mass is calculated from870 μm as listed in Hodge et al. (2013) (primary-beam-corrected flux, column 8 in Table 3) and by combining it with the information (i.e., $M_\star$, SFR, redshift) from another SED fitting (i.e., MAGPHYS) presented in da Cunha et al. (2015). The redshift of the main sequence SMGs is restricted to $z < 3$ since the 870 μm flux above $z > 3$ no longer traces the RJ tail,

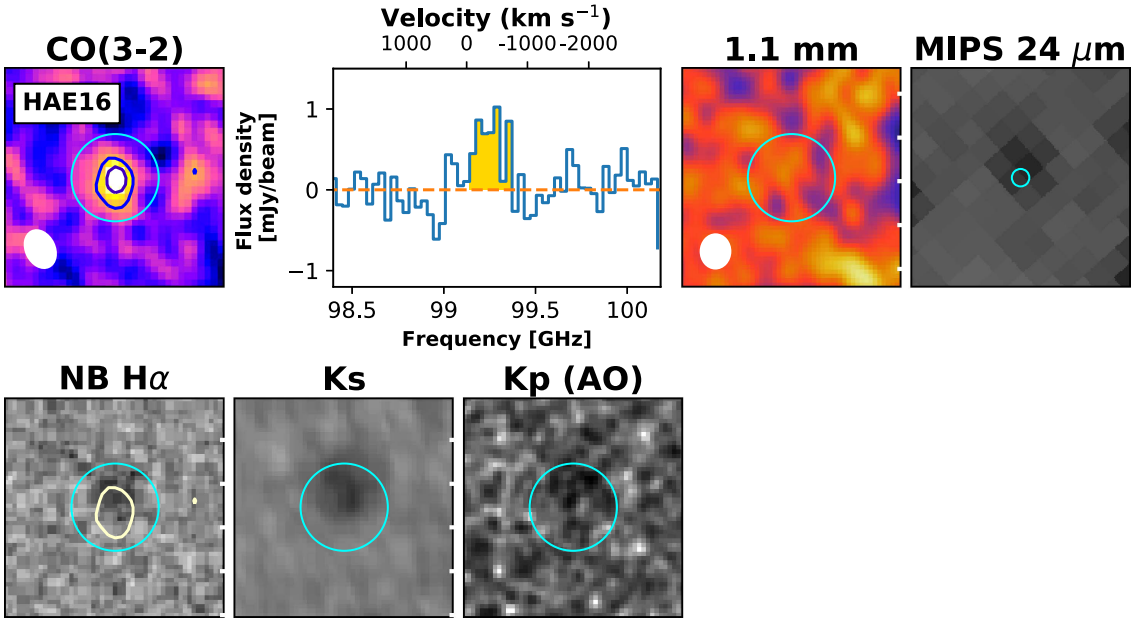

Figure 7. Multi-band images for the galaxies having either CO (3–2) or 1.1 mm detection (continued) for HAE16. Refer to Figure 4 for the description of each panel and symbol.

producing large uncertainties in the estimation of gas mass for the analysis of S16.

5.3. Combined Results of SFR versus $M_{\rm gas}$

The gas masses derived from different estimators of CO (3–2) and 1.1 mm are roughly consistent with each other; three HAEs (HAE3, HAE8, and HAE9) are roughly consistent within errors, and the $M_{\rm gas,dust}$ of HAE10 is less than $M_{\rm gas,CO}$. The latter case might be related to the variation of the dust-to-gas ratio (thus metallicity) and optically thin CO emissions, which are difficult to entangle with the given data (see Section 6.3 for a discussion).

A tension between two estimators may still exist. The gas mass derived from 1.1 mm is systematically smaller for all four cases, even though the sensitivity limit of the 1.1 mm observations is deeper in terms of the gas content with the prescription of S16 (see also Section 6.3).

We will focus on the results of CO (3–2) since the detected number is larger. We perform a comparison with other surveys (those presumably in general fields), mainly the results of G15 and Tacconi et al. (2017) in which the scaling relation of gas depletion time and molecular gas fractions in general fields was derived from CO (3–2) measurements.

Apparently, a systematically different correlation (anti-correlation with Pearson's correlation coefficient $r = -0.85$ with a p-value of 0.01) between SFR and $M_{\rm gas}$ is found in protocluster members, even though the median SFE is consistent with the average value of PHIBBS samples at similar sSFR values ($\langle {\rm SFE} \rangle \sim 1.8\,{\rm Gyr}^{-1}$; Figure 8). We discuss the issue further in Section 6.2 but note here that the apparent anti-correlation is mainly due to two populations: (1) AGN-dominated HAE5 and (2) less massive galaxies among the detected galaxies, i.e., HAE9 and HAE16 with large velocity widths, in which the uncertainties of SFR from Hα is expectedly larger than those in other cases. Additionally, such anti-correlation (or no correlation) is observed in the ALESS SMGs on the main sequence with less significance ($r = -0.43$ with p-value $= 0.13$). We investigate the anti- (or no) correlation in the discussion section, and the difference might hint at an environmental effect of galaxy evolution during cluster formation.

In relation to this result, we note that all galaxies detected in CO (3–2) have been detected in MIPS 24 μm (Figures 4–7). The natural correlation between the total ISM content (traced by CO (3–2)) and star-forming activity (traced by 24 μm) (=KS relation) supports this idea. The MIPS 24 μm emission at this redshift traces the rest-frame 7.7 μm and 6.2 μm polycyclic aromatic hydrocarbon (PAH) features (for the main-sequence galaxies), and the flux can be interpreted as the SFR of the galaxy (Lagache et al. 2004). However, the 24 μm flux can also be a tracer of the warm dust component heated by an AGN (Rigby et al. 2008). HAE5 with a broad-line AGN signature (Tanaka et al. 2011) is an example that might weaken the positive correlation. An environment that may result in a weak correlation (with large scatter) is a place of intense radiation field, for example, the (compact) galaxies with high IR luminosity (i.e., starbursts; e.g., Elbaz et al. 2011). The 24 μm flux may also be reduced in low metallicity and a hard radiating field (if any; e.g., Shivaei et al. 2017). All these related factors will be further discussed in subsequent papers.

5.4. Gas Fraction

We calculated the gas fraction ($f_{\rm gas} = M_{\rm gas}/(M_{\rm gas} + M_\star)$) from the estimated gas mass and the stellar mass. The average value of the gas fraction is $\langle f_{\rm gas} \rangle = 0.55 \pm 0.07$ for CO (3–2) and 0.50 ± 0.06 for 1.1 mm, and the values are roughly consistent with each other.

We found that the gas fraction strongly depends on the stellar mass, as in the PHIBBS-I sample (Figure 9). Such a mass dependency of gas fraction may be regulated by the mass-dependent feedback and/or the gas accretion efficiency as

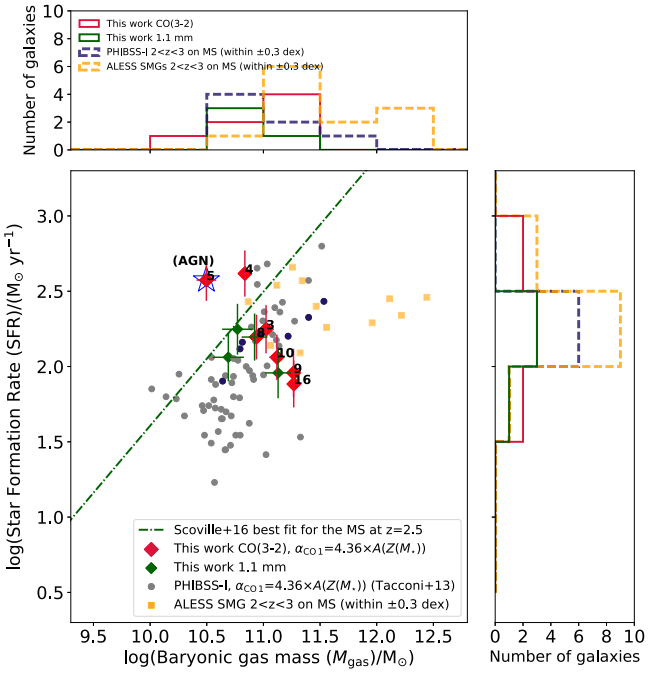

Figure 8. Derived molecular mass distribution with respect to SFR. The molecular mass is derived from CO (3–2) (red diamonds) or dust-continuum (green diamonds) detection (see Section 5 for details). HAE5 is indicated with a star symbol to clarify the existence of AGNs, the SFR of which, derived from the Hα emission, may be overestimated. We also plot other high-z molecular and dust-continuum survey results from PHIBBS-I (Tacconi et al. 2013), galaxies in the COSMOS field S16 and ALESS (Hodge et al. 2013; da Cunha et al. 2015) by applying the same analysis on $M_{\rm gas}$ (but not for SFR or $M_\star$). The PHIBBS-I survey (gray circles) is based on the CO(3–2) measurements for star-forming galaxies on the main sequence. We indicated in dark blue the PHIBBS-I galaxies that are massive ($M_\star > 4 \times 10^{10}\ M_\odot$) on the main sequence ($\pm$0.3 dex) within $2 < z < 3$. S16 (dashed green line) is based on the dust-continuum (Band 7 at 870 μm) observation. The ALESS survey is also observed at the 870 μm continuum by using ALMA, but the observation was made toward LESS SMGs found in the ECDF-S field. Yellow squares are massive ($M_\star > 4 \times 10^{10}\ M_\odot$) SMGs on the main sequence within $2 < z < 3$. At a given SFR, the gas content is roughly consistent with PHIBBS-I, while ALESS SMGs on the main sequence have a higher gas content, perhaps because of the nature of its selection.

previously addressed in cosmological hydrodynamical simulations (e.g., Figure 11 in Tacconi et al. 2013, which uses Davé et al. 2011). We will additionally discuss in the following section the potential role of the environment in this picture. However, we note that Figure 9 is also consistent with the gas mass fraction spanning the entire range, just from the stochastic nature of inflow and star formation; after all, the gas depletion time is short for any coherent evolutionary scenario.

We compared the above results with PHIBSS-I and ALESS SMGs particularly for those on the massive ($>4 \times 10^{10}\ M_\odot$) main sequence at $2 < z < 3$. By restricting galaxies in PHIBBS-I, which results in only seven galaxies for comparison, we find that the average gas fraction does not differ ($\langle f_{\rm gas,PHIBBS-I,MS}\rangle = 0.49 \pm 0.05$; bottom of Figure 10). Other studies on the main-sequence galaxies have revealed similar results (e.g., Magdis et al. 2012; Saintonge et al. 2013; Sargent et al. 2014; Scoville et al. 2014; S16; Decarli et al. 2016a; Schinnerer et al. 2016). ALESS SMGs on the massive main sequence at $2 < z < 3$ (total number of 13) appear to have a slightly higher mean value ($\langle f_{\rm gas}\rangle = 0.64 \pm 0.07$; Figure 10 top) but is nevertheless consistent within an error.

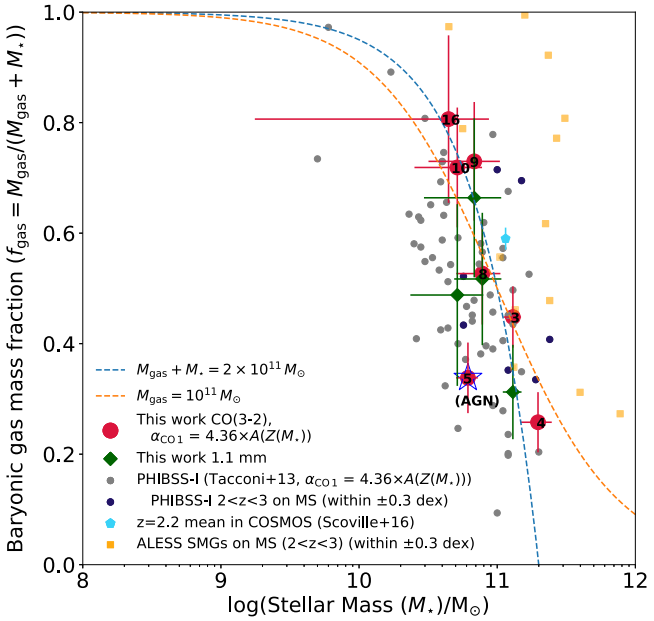

Figure 9. Gas fraction ($f_{\rm gas} = M_{\rm gas}/(M_{\rm gas} + M_\star)$) as a function of stellar mass ($M_\star$). The same color scheme is used in Figure 8 for HAEs in the protocluster, PHIBBS-I, and ALESS SMGs on the main sequence. The result from Scoville et al. (2016) for $\langle z\rangle = 2.2$ mean is plotted with the cyan pentagon. At a given stellar mass, the protocluster members have similar gas fraction distributions with those in general fields.

6. Discussions

6.1. Reasons for Unexpected Non-detection

Out of the seven CO(3–2) detections, only four have 1.1 mm counterparts. We could not detect 1.1 mm emission for HAE4, HAE5, and HAE16. Massive galaxies with $M_\star > 10^{11}\ M_\odot$ (HAE1, HAE2) that have high SFRs from the Hα emission and other galaxies with high SFRs (HAE12, HAE13) are not detected in either the CO (3–2) or 1.1 mm emissions, as opposed to our expectation that these galaxies would be detected if the normal KS relation applies. Furthermore, recent observations reported the detection of the massive main-sequence galaxies (e.g., Decarli et al. 2016b; Tadaki et al. 2017). There are several reasons that may apply for the non-detection.

1. AGN-dominated galaxies (HAE1 (radio galaxy 4C23.56) and HAE5): although the Hα emission detected by the NB filter may have a significant contribution from AGN so that the intrinsic SFR may be smaller than the estimated SFR, the AGN-dominated galaxies may be intrinsically gas-poor systems because of the AGN feedback, i.e., energetic outflows blowing out the gas content (e.g., Cicone et al. 2014). HAE5, detected only with CO(3–2), has one of the lowest gas contents and gas fractions. Since the radio galaxy has gigantic bipolar radio lobes associated with the X-ray emissions (Blundell & Fabian 2011), another possibility is the lack of a "cold" phase gas, such as that traced by cold dust (i.e., $T_{\rm d} = 25$ K) and low-J CO emissions that we observed, owing to a strong radiation field heated by the central AGN.
2. Intrinsically smaller $M_\star$ and SFR (HAE2): from our newly obtained AO-data, we found that the galaxy may be gravitationally lensed. The intrinsic stellar mass (and

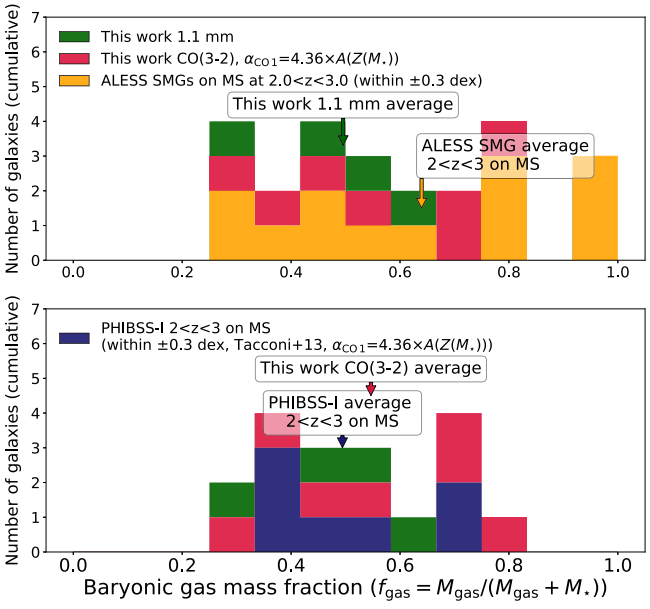

Figure 10. Histogram of gas mass fraction for the massive ($>4 \times 10^{10}\,M_\odot$) main-sequence galaxies at $2 < z < 3$. We plot the distribution of the ALESS SMGs on the top panel and that of PHIBSS-I on the bottom. In general, the distribution of gas fraction (scatter $\sigma_f = 0.20$ for CO (3–2) and $\sigma_f = 0.12$ for 1.1 mm) and the average ($\langle f_{gas}\rangle = 0.55 \pm 0.07$ for CO (3–2) and 0.50 ± 0.06 for 1.1 mm) of the protocluster galaxies are consistent with PHIBBS-I ($\langle f_{gas}\rangle = 0.49 \pm 0.05$, $\sigma_f = 0.14$), but with a slightly larger scatter ($\sigma_f = 0.24$) and average ($\langle f_{gas}\rangle = 0.64 \pm 0.07$) for ALESS SMGs on the main sequence. SMGs have a slightly higher value, perhaps because of the selection effect.

SFR) may be much less than expected from the seeing-limited data (I. Tanaka et al. 2017, in preparation).

3. Extended low surface brightness dust component (HAE4)?: the non-detection in 1.1 mm with CO(3–2) detection might suggest a lower surface brightness in the dust continuum, which is also discussed in Decarli et al. (2016b) for a galaxy that has no dust but is detected in CO. Because HAE4 has greatly extended Hα emission compared to CO (see Figure 4), the dust might also be extended and diffuse. It is unlikely from a general point of view, however, that local U/LIRGs as high-z analogs (in terms of IR luminosity) have a compact dust component with high surface brightness (e.g., Sakamoto et al. 2013; Saito et al. 2015) compared to CO emissions. Future observation is necessary to confirm such populations.
4. The lack of sensitivity (HAE16): HAE16 is observed at the edge of the FoV at Band 6, and the sensitivity was not sufficient to detect dust continuum, given the CO (3–2) detection.
5. Lower metallicity for low stellar mass galaxies?: HAE12[24] and HAE13 have high SFR but in the relatively lower mass ($<10^{10}\,M_\odot$) regime. The gas may be CO-dark in terms of the effect of photodissociation in the low-metallicity regime. The dust-based calibration might no longer be valid. Otherwise, they are gas-poor systems with high SFE.

[24] Additionally, we note that the galaxy is in the close vicinity of the radio galaxy (offset ~25 kpc physical size). The galaxy might have encountered a strong feedback from the AGN, for which we need additional observations.

All the potential cases we have listed have to be checked with future observations with increased depth and higher resolution to confirm the diversity of cold gas properties of the protocluster members.

Our findings also suggest caution regarding general expectations for the main-sequence galaxies. With the variety of potential reasons for unexpected non-detection of the protocluster galaxies on the main sequence, "some universality" of the main sequence may have to be carefully re-checked through observations. There is a wide range of gas content and SFR with different masses.

6.2. Additional Adjustment in Dust Extinction?

Since we adopt only mass-dependent extinction correction using Garn & Best (2010), we need to carefully consider whether the corrected SFR from Hα is accurate.

Considering the averaged value of a galaxy population as a whole, we find that the correction method appears to be adoptable for ALMA detected galaxies. We have tested with other results derived using an extinction-free radio flux (e.g., Kennicutt & Evans 2012) with Jansky Very Large Array (JVLA) observations at 3 GHz (10 cm; Lee et al. 2015; M. Lee et al. 2017, in preparation). We find that the difference is within a few factors ($\lesssim 4\times$) between the SFRs adopted in this paper and that derived from the radio flux, suggesting that they are not extremely (i.e., $A_v \gg 5$) obscured cases that relocate a galaxy well above the main sequence (i.e., $\geqslant$0.6 dex) but are moderately dusty. Exceptional cases are radio-loud AGNs in which the radio flux overestimates SFR owing to the increased contribution of non-thermal synchrotron emission from the AGN, which no longer traces star-formation activities of a galaxy. The differences of individual galaxies canceled out and star-formation rate are, on average, roughly consistent with each other.

Nevertheless, we need to pay careful attention, given the limited number of detections with limited range (~an order of magnitude) of the parameter space (i.e., M_*, SFR, M_{gas}). Particularly, the radio measurements show the SFRs of HAE16 and HAE9 (those with the highest f_{gas}) to be ~3–4 times larger than SFR_{H_α} (corrected). They will be re-located slightly above or on the upper edge of the main sequence (HAE16: log ($sSFR_{JVLA}/sSFR(ms)$) ~0.4 dex; HAE9: log($sSFR_{JVLA}/sSFR$ (ms)) ~ 0.3 dex) since they were on the lower edge of the main sequence with Hα-based measurements (see Figure 1). If we adopt the radio measurements instead, with higher SFR for HAE9 and 16, the apparent "anti-correlation" between SFR and M_{gas} observed in Figure 8 becomes less significant, though it still exists.

The radio observations are also limited by the detection number and have a significant scatter with the uncertainty in the radio spectral index. Further investigation will be conducted in future studies but is beyond the scope of this paper. Therefore, our best conjecture for the intrinsic star-formation rate within this paper is the use of $SFR_{H\alpha}$ (corrected) while considering the potential uncertainty for the extinction correction.

6.3. Validity of Using the Galactic Conversion Factor

Many studies of typical star-forming galaxies, particularly in the high-mass region where the metallicity dependence is low, have adopted the "Galactic" CO (1–0)-to-H_2 conversion factor (e.g., Dickman et al. 1986; Daddi et al. 2008, 2010; Tacconi et al. 2013;

G15), and the U/LIRG-like conversion factor $\alpha_{CO} = 0.8$ $M_{\odot}$ (K km s^{-1} pc^2)$^{-1}$ is used for galaxies above the main sequence at a high redshift (e.g., Solomon & Vanden Bout 2005; Yun et al. 2015).

Our findings suggest that the use of $\alpha_{CO} = 4.36$ ($M_{\odot}$ (K km s^{-1} pc^2)$^{-1}$) as the first order is favorable for the protocluster galaxies on the main sequence. It renders the gas masses derived from different calibrations, i.e., CO(3–2) and dust continuum, consistent with each other within errors. The U/LIRG-like conversion factor yields larger inconsistencies between different estimators since the gas mass derived from CO is smaller than dust measurement by a factor of two to five. If it were applicable, this would require a higher dust temperature, higher by a factor of two to five, since the gas mass recipe of Scoville et al. (2014, 2016), the gas mass is inversely proportional to the dust temperature (i.e., higher RJ correction factor Γ_{RJ} with increasing dust temperature). Such a high dust temperature is unlikely at the observed resolution. The observed resolution and the size (measured when it is resolved) can probe the average temperature of the galaxy as a whole. Otherwise, it would be extremely compact (<1 kpc) in size.

Provided the small number of detections, we may be able to examine further the validity of adopting the "Galactic" conversion factor, when (1) larger samples (with a larger mass range) and (2) different measurements (e.g., multiple-J CO line or a simpler optically thin line such as [CI]) are available.

Before closing this section, we list several considerations for the adoption of the conversion factor.

1. Large line width: we found that more than two-thirds of galaxies have velocity widths >300 km s^{-1}, i.e., very disturbed similar to on-going mergers observed in local U/LIRG (M. Lee et al. 2017, in preparation). In this case, CO emission might be optically thin, requiring the conversion factor to be lower than the assumed value. We note, however, that in Daddi et al. (2010), six BzK galaxies detected with CO(2-1) have large FWHM (>500 km s^{-1}), and the authors used the "Galactic" value; one of the six galaxies is possibly a rotating disk in the velocity-position diagram, while the others cannot be directly tested to determine whether they are rotating.
2. Uncertainties in the contribution of atomic content: we assumed that the molecular gas is dominant in high-z galaxies since the mean H_2 column densities and ISM pressure are expectedly higher than the local values (e.g., Obreschkow et al. 2009). Furthermore, because a protocluster is similar to a group-like environment (e.g., Toshikawa et al. 2014), shock heating might prevent H I gas from accreting onto a galaxy (e.g., Appleton et al. 2013) or the neutral gas may be stripped while galaxies form a common halo (e.g., Verdes-Montenegro et al. 2001) leading to a lower H I content compared to that of the fields. In addition, the gas accreted particularly onto massive galaxies around high-z overdensities may be recycled gas (Emonts et al. 2016).
3. Gas mass from CO is always higher than that derived from 1.1 mm: we find a systemic offset between CO-based and dust-based measurements, and a similar trend was previously reported from several studies (e.g., Genzel et al. 2015; Decarli et al. 2016b). Genzel et al. (2015) argued that referring to the true dust temperature (at least from two bands) and correcting for metallicity would improve the inconsistency. It might also be due to the more extended and diffuse nature in 1.1 mm, where the extended emission below the surface brightness limit is missed (see also Section 6.1).

Additionally, we have discussed the validity of the "Galactic" conversion factor from the dynamical mass point of view that includes large uncertainties without measuring the size and inclination (see Appendix C). We will revisit this issue with future observations.

6.4. Gas Content in a Protocluster

We find that our protocluster members have, on average, similar gas fractions of main-sequence field galaxies (see Figures 9 and 10). The ALESS SMGs on the main sequence may have slightly higher gas fractions, but they are consistent within errors. Since ALESS SMGs were pre-selected by their dusty nature, i.e., bright SMGs in the LESS sample (Hodge et al. 2013), gas-rich main-sequence galaxies may have been selectively chosen. In either case, the gas fractions for all of the high-z galaxies are higher than the local value (of star-forming galaxies, $f_{gas} \sim 0.08$) at a given stellar mass (e.g., Saintonge et al. 2013; Tacconi et al. 2013).

We estimate the cosmic gas density of the protocluster (Figure 11). The survey area is 14 comoving Mpc^2, and we adopted an ~20% sensitivity region (a radius of 37″) with our four-pointing observations. If Δz is restricted only to the sources detected in CO (3–2), which results in the range of $2.478 < z < 2.487$ (~11 comoving Mpc), then the cosmic gas density is estimated as $\rho_{gas,4C23.56} \sim 5 \times 10^9\, M_{\odot}$ Mpc^{-3}.

This is ~22× higher than the upper limit of the general field, i.e., HUDF at $z = \langle 2.6 \rangle$ (Decarli et al. 2016a) or other previous surveys (Walter et al. 2014; Keating et al. 2016) and any other models (e.g., Obreschkow & Rawlings 2009; Lagos et al. 2011; Sargent et al. 2014). Note that we applied the same $R_{13} = 2.38$ and the uniform conversion factor $\alpha_{CO\,1} = 3.6$ to compare with the result of Decarli et al. (2016a). This effectively changes the total value of $\rho_{gas,4C23.56}$ by ~15%.

Provided a recent simulation with an expected size of the protocluster (Chiang et al. 2013), we could perform a more conservative derivation assuming a wider redshift range. We performed calculations by assuming the line-of-sight distance of the protocluster to be set by the narrow-band filter coverage ($\Delta z \sim 0.03$, ~40 comoving Mpc). The gas density becomes $1 \times 10^9\, M_{\odot}$ Mpc^{-3}, which is still a factor of six higher than the result of general fields. A more conservative method is to derive the gas density by applying a U/LIRG-like conversion factor for all detected sources, lowering the gas density by a factor of 4.5, which can be regarded as the lower limit of the gas density of the protocluster, close to the upper limit of the general field.

Although it may not be fair to compare our results with the results of *Subaru*/MOIRCS, which has a different survey size (~3000 comoving Mpc^3), we note that protocluster 4C23.56 is also an order of magnitude higher in the cosmic star-formation-rate density (SFRD) and (3–9) times higher in the stellar mass density ($\rho_{\star}$) compared to the results presented in Madau & Dickinson (2014) with the detection of 25 HAEs.

We barely infer the causality of these observational results. The higher gas density may simply be due to the higher number density of the galaxies at a given volume, which can also be

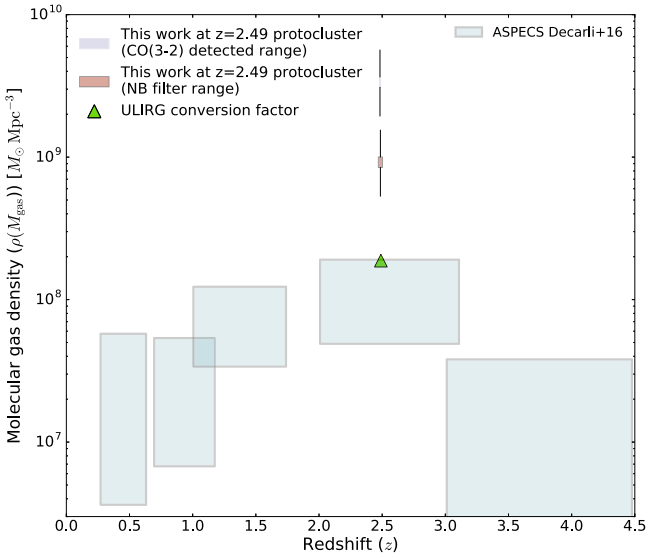

Figure 11. Cosmic gas density for the $z = 2.49$ protocluster (this work) overlaid on the recent ALMA studies of the general field, HUDF-S (Decarli et al. 2016a; see the text for details of the calculation to match both results). We plot three different estimations (1) using the CO(3–2) redshift range ($\Delta z \sim 0.01$), (2) using the NB filter redshift range ($\Delta z \sim 0.03$), and (3) applying the U/LIRG conversion factor ($\alpha_{CO} = 0.8$ for the case (2). The black error bar is estimated by taking into account Poisson uncertainties (Gehrels 1986).

inferred from the high SFRD and $\rho_\star$. Alternatively, the reason for the galaxy overdensity in the protocluster might be the higher gas density within the volume. The former case can be simply explained by the number density of HAEs of the protocluster being threefold higher than that of the field (Tanaka et al. 2011) and the fact that the average gas fraction is similar to the field.

However, we note that the estimated gas density is the lower limit since we only perform calculations for the detected sources. It is uncertain whether galaxies at a lower mass regime have a larger amount of gas, and this issue cannot be clarified with the current method (or current calibration). Nevertheless, we did find an extremely large amount of gas ($f_{gas} > 0.7$) in three of the galaxies, HAE9, HAE10, and HAE16, which are in the lower massive bin in our detected sample. While noting that statistical significance is not sufficiently high to reject the opposing case given the size, the scatter of the gas fraction (observed in CO (3–2)) is 13% higher than that of the PHIBBS-I sample. Further higher sensitivity observations or another tracer of the so-called CO-dark gas tracers would clarify this issue.

6.5. Environmental Effect during the Cluster-forming Epoch?

6.5.1. Detection in the Densest Region

Motivated by the discovery of the morphology–density relation in Dressler (1980) and the relatively secure redshift ranges for the HAEs from the NB technique, we may regard the surface density as an indirect and rough representation of the cosmic web.[25] The surface galaxy number density is measured by applying Gaussian kernels with a radius of 0.′8 (∼1.4 comoving Mpc) and calculating the galaxy number within the area (Figure 2).

Among seven CO-detected galaxies, five HAEs are located in the region of highest surface density. We note that the number density of HAEs within the protocluster is three times larger than general fields (Tanaka et al. 2011; I. Tanaka et al. 2017, in preparation). We plot the protocluster galaxies detected in Figure 12 and colorize them to show the (relative) surface galaxy number densities, where the numbers next to the color bar are shown in the unit of arcmin^{-2}.

This suggests that the CO (3–2) (or dust) detection of the galaxies depends on (but not necessarily) the large-scale structure. Umehata et al. (2015, 2017) argued that there is a concentration of the 1.1 mm continuum sources in the node of protocluster SSA22, where filamentary structures meet. If it also applies to our case, the detection in the region of highest surface density may be mirroring the preferential place of gas detection within certain large structures of the protocluster, e.g., projected filaments or the node, where the gas is infalling or being accreted. Future mapping observations of gas content are necessary to visualize such phenomena, which will allow us to reveal environmentally driven galaxy evolution with a differential gas supply (and consumption) at a high redshift.

If we focus on these five galaxies, they are again divided into two populations: (1) a vast amount of gas with a relatively low mass ($f_{gas} \gtrsim 0.7$, $4 \times 10^{10} < M_\star/M_\odot \lesssim 1 \times 10^{11}$) in relatively less dense regions (HAE9, HAE10, and HAE16) and (2) more massive galaxies ($\gtrsim 1 \times 10^{11}$) with lower $f_{gas} \lesssim 0.5$ in denser regions (HAE4 and HAE8).

6.5.2. Comparison with Previous Studies

To discuss further, we compare our results with recent results presented in G15 and S16, in addition to our analysis of the ALESS SMGs on the main sequence and PHIBBS-I. G15 enlarged the sample size by including the results of not only the PHIBBS-I galaxies but also PHIBBS-II, IRAM-COLDGASS, and other surveys. Recently, Tacconi et al. (2017) presented extended work. From these extensive studies, a scaling relation of the depletion time ($\tau_{depl.}$) is empirically derived. The gas depletion time can vary with the redshift (z), offset from the main sequence Δ(MS) and dependency of stellar mass ($M_\star$). We use the empirical fit of G15 and plot the expected line on the plane of f_{gas} versus sSFR in Figure 12 by considering the definition of f_{gas}. The gas fraction can be equated with sSFR and $\tau_{depl.}$, i.e., $f_{gas} = 1/(1 + (\mathrm{sSFR} \times \tau_{depl.})^{-1}$. By definition, at a fixed sSFR, f_{gas} decreases with decreasing $\tau_{depl.}$. We also fill an area using the characteristic depletion time $\tau_{depl.} = 200$–700 Myr for high-z galaxies, as presented in S16, to show how f_{gas} changes as a function of sSFR with this depletion time range.

Our targets and control samples (PHIBBS-I, ALESS SMGs on the main sequence) are within a narrow range near the main sequence. Therefore, at an almost fixed sSFR, the scattered points (the protocluster members, PHIBBS-I and ALESS SMGs on the main sequence) around the results of G15 and S16 can be regarded to indicate the dependence on the global SFE or $\tau_{depl.}$ (Figure 13).

By excluding AGN (HAE5), our results give a positive correlation between $M_\star$ and SFE (Pearson's correlation coefficient (in log scale) = 0.89 with a p-value of 0.02), and such a relation perhaps decreases the f_{gas} of massive galaxies, in contrast to the empirical fitting in G15 and Tacconi et al. (2017), and the

[25] If it were available, it would be better to discuss with 3D volume density. However, the number of galaxies is still too small to find a particular structure in 3D.

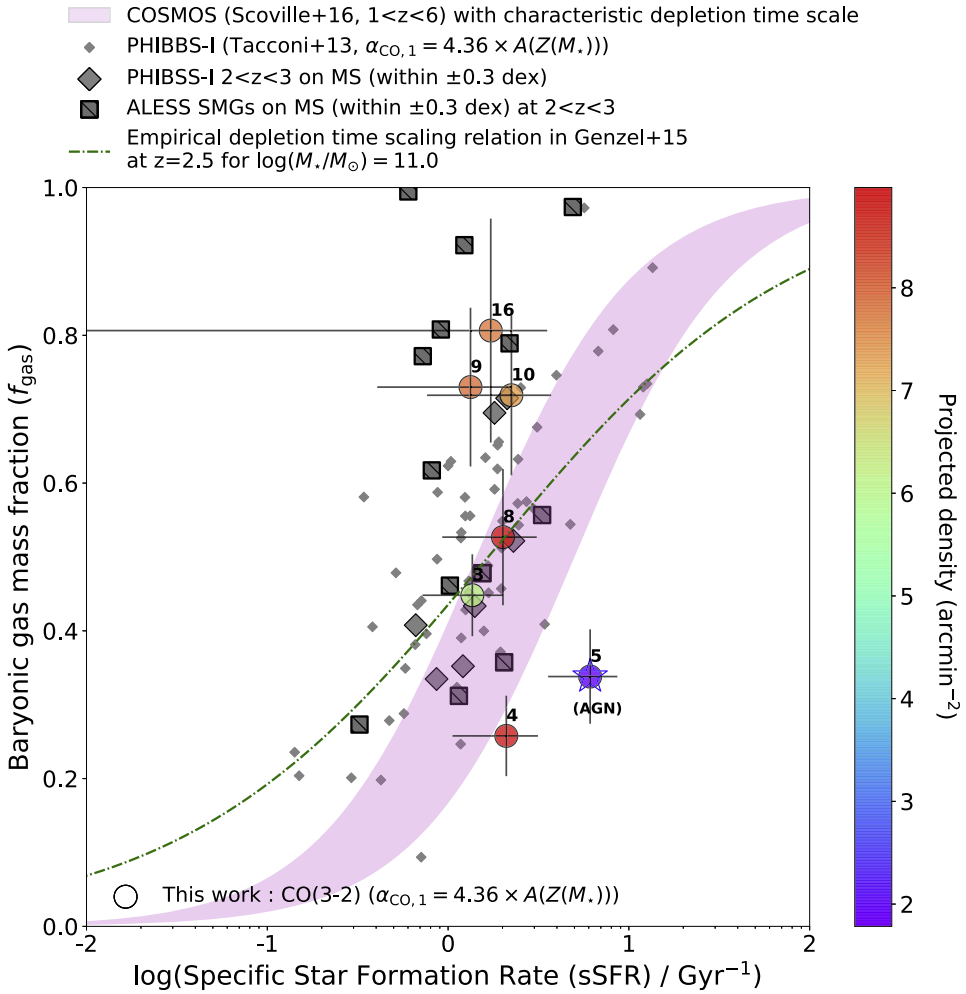

Figure 12. Gas fraction as a function of specific star-formation rate. The color bar and numbers next to it show the relative surface number density of galaxies in $arcmin^{-1}$. The surface number density is estimated by the method described in the caption of Figure 2 and in the text. We plot an empirical model of scaling relation on the depletion time described in G15 by fixing the redshift at $z = 2.5$ and the stellar mass$M_\star = 1 \times 10^{11}\,M_\odot$. For comparison, the massive ($>4 \times 10^{10}\,M_\odot$) main-sequence galaxies at $2 < z < 3$ are plotted from PHIBBS-I (gray diamonds) and ALESS (gray hatched squares). We plot the results of Scoville et al. (2016) by using the characteristic depletion time of $(2 - 7) \times 10^8$ years. A star symbol indicates the existence of AGNs.

PHIBBS-I galaxies. The latter cases show a weak negative (or flat) correlation between $M_\star$ and SFE. Although the intrinsic SFR of non-AGN, dusty galaxies (e.g., HAE9 and 16) might be higher than SFR_{H_α} (corrected; Section 6.2), a positive correlation nevertheless holds (but becomes rather weaker). One may argue that such an apparently different correlation from the general field is only due to the sample bias and is still explained within the scatter of the PHIBBS-I sample. We cannot reject this argument with the current data set. This issue can only be investigated through larger and deeper observations by collecting statistically large numbers. However, we note that the SFE dependency of the stellar mass (and thus gas fraction) appears to have some connection with the galaxy number density (Figure 12) and, thereby, perhaps with the environment, as shown in the previous section.

6.5.3. Suggested Picture and Future Aspects

The correlations shown in the previous sections suggest some insight into massive galaxy evolution and the properties of dark matter within a high-z protocluster.

As discussed in Genzel et al. (2015; Section 4.3), the global depletion time can be related to dark-matter properties in the framework of disk formation within a dark-matter-dominated universe (Mo et al. 1998 see also Equation (24) in G15): the baryons' angular-momentum parameter (λ), galaxy's (local) star-formation efficiency (η), dark-matter concentration parameter (C_h), and Hubble parameter ($H(z)$). The similarity of the averaged physical properties for the galaxies on the main sequence may be due to two dominant factors between the balance of $H(z)$ and perhaps η. The mass dependency of SFE (at an almost constant sSFR) suggests that additional (or different) physical processes, which are perhaps related to the environment, are necessary to explain this phenomenon. Considering that halo concentration is higher in denser environments and increases in later times (Bullock et al. 2001) and that a (proto) cluster is a place where galaxy evolution proceeds earlier (e.g., having a quenched or passive population at the center in advance; Kurk et al. 2009; Strazzullo et al. 2013; Koyama et al. 2014; Cooke et al. 2016), the halo concentration parameter of the most massive galaxies in denser regions might be higher than that of less massive galaxies in less dense regions, which should be tested with future observations.

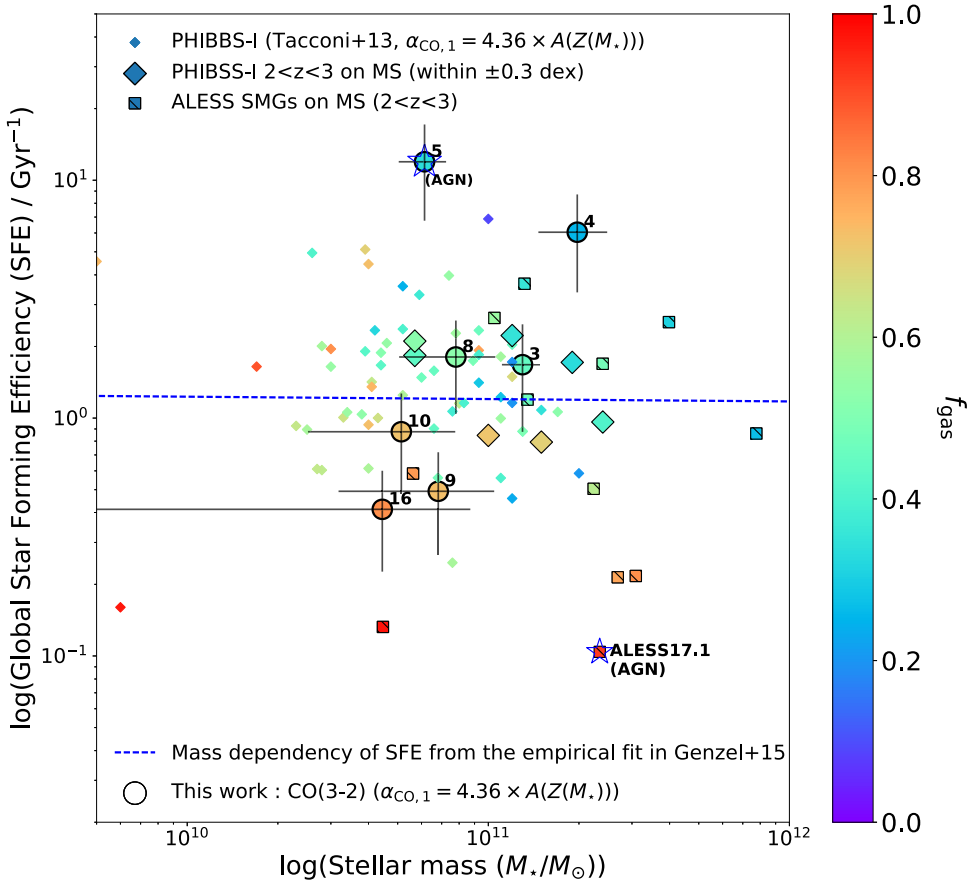

Figure 13. Stellar-mass dependency of global star-forming efficiency. Although the probed range is still narrow, a positive correlation between $M\star$ and SFE is found for the protocluster galaxies, in contrast to the result of Genzel et al. (2015) for the main-sequence galaxies. The empirical fitting formula presented in Genzel et al. (2015) shows a small dependency (with a power of 0.01) on stellar mass in the depletion timescale (i.e., a power of −0.01 for SFE indicated by the dashed line) compared to the larger contributions of the deviation from the main-sequence sSFR and the redshift evolution. The color scheme shows the f_{gas} for individual galaxies. A star symbol indicates the existence of AGNs.

However, we note that the CO line widths tend to decrease with increasing stellar mass (and thereby f_{gas} (Table 1 or see the spectra in Figures 4–7) and SFE), hinting at a change of the angular-momentum parameter, which needs to be investigated with future higher-resolution observations with a constraint on the inclination. Considering the total gas content is almost constant, as shown in Figure 9 for the detected sources, this further shows a signature of changes in the dark-matter fraction. A test on the timescale of these changing parameters, is additionally required through both observations and simulations. A quantitative estimation of all of these contributions may not be simple, but it is certainly required in future observations for understanding the environmental effect in galaxy evolution at high z.

The proposed picture, however, may be different for galaxies with stellar mass less than $10^{10}\,M_\odot$, provided non-detection, and they have to be investigated via deeper observation. Thus far, there is little evidence for the change of the scatter of the main sequence in a different environment (e.g., Peng et al. 2010; Koyama et al. 2013; Darvish et al. 2016), but recently, Hayashi et al. (2016) reported a larger (upward) scatter of main-sequence galaxies in the low-mass galaxies ($<10^{9.3}\,M_\odot$) at the $z = 2.5$ protocluster, which is in fact similarly seen in our sample (I. Tanaka et al. 2017, in preparation; see Figure 1).

7. Conclusion

In this paper, we investigated the gas content of HAEs that are typical star-forming galaxies on the main sequence associated with protocluster 4C23.56 at $z = 2.49$. To derive the gas properties, we conducted CO (3–2) (Band 3) and 1.1 mm ($\lambda_{rest} \sim 385\ \mu$m) dust-continuum (Band 6) observations with ALMA toward the protoclusters for which panchromatic studies are available. This is the first paper in a series of papers that reveal the gas properties of galaxies within the protocluster. From the ALMA observations, our results are as follows.

1. We obtained seven CO (3–2) and four 1.1 mm dust-continuum detections. All four 1.1 mm detections are included in CO (3–2) detections. While the parent galaxies have a stellar mass range greater than three orders of magnitude ($\log(M_\star/M_\odot) = [8, 11.5]$), the detected sources are all massive ($M_\star > 4 \times 10^{10}\ M_\odot$) on the star-forming main sequence.
2. Gas mass was derived using the "Galactic" conversion factor with additional correction for the metallicity dependence of the CO conversion factor using the method described in Wuyts et al. (2014) and following the analysis presented in Genzel et al. (2015) for CO (3–2), which yields a consistent value derived from dust-based calibration using Scoville et al. (2016).

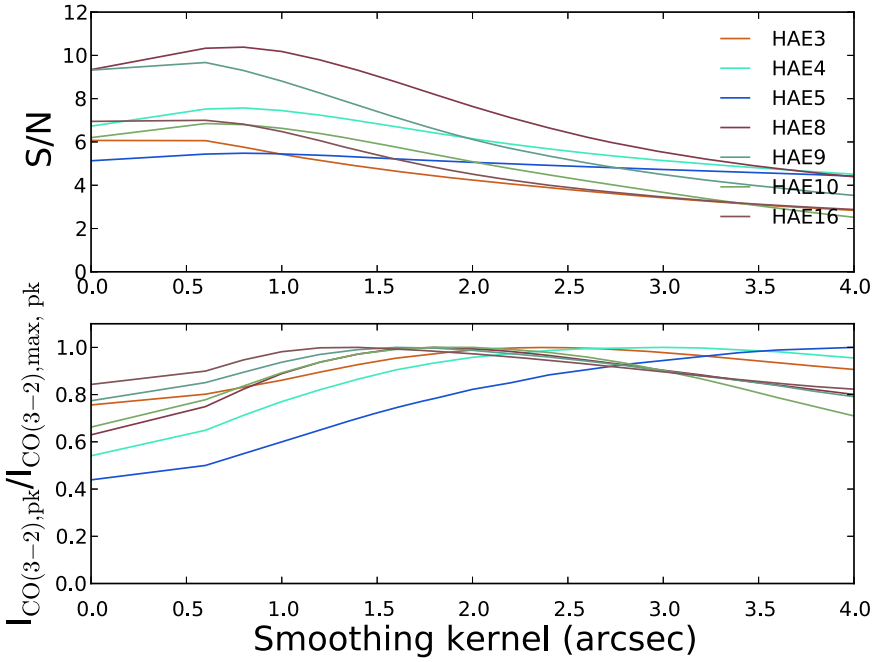

Figure 14. S/N and peak flux growth curve in Band 3. We need to consider both S/N and flux to optimize the smoothing parameter to estimate a total flux. We have chosen a kernel of $0\farcs6$ to conduct a uniform analysis with Band 6 data as well. At this kernel, the expected flux recovered at least 50% of the maximum flux (but with low S/N).

3. The HAEs having either CO (3–2) and 1.1 mm detection carry, on average, a gas mass content similar to those of main-sequence galaxies in general fields. The massive HAEs ($M_\star > 4 \times 10^{10}\ M_\odot$) have a gas content in the range of (0.3-1.8) $\times 10^{11}\ M_\odot$ and a median gas fraction $\langle f_{\rm gas}\rangle = 0.53 \pm 0.07$ for CO (3–2) and 0.50 ± 0.06 for 1.1 mm measurement. Including our work, the high-z massive galaxies ($2 < z < 3$) on the main sequence that were considered (Hodge et al. 2013; Tacconi et al. 2013; da Cunha et al. 2015; S16) all possess a higher gas content than those of local star-forming galaxies, regardless of their environment.
4. The cosmic gas density of high-z protoclusters was measured for the first time. Using either the redshift range of CO (3–2) ($\Delta z \sim 0.01$) or the NB filter ($\Delta z \sim 0.03$), which is comparable to the predicted size in simulations (e.g., Chiang et al. 2013), and the survey area of Band 3, we found an enhancement of cosmic gas density, $\rho_{H_2} \sim$ (1–5) $\times\ 10^9\ M_\odot\ {\rm Mpc}^{-3}$, that is already a factor of 6-22 higher in value only with the detection than the upper limit set by the recent survey toward HUDF (Decarli et al. 2016a) with the same assumption of conversion factor and line ratio.
5. We found that $f_{\rm gas}$ decreases with increasing stellar mass, as observed in control samples. However, our sample differs in that $f_{\rm gas}$ also changes with surface galaxy number density. Galaxies with a higher gas fraction ($f_{\rm gas} > 0.7$) are less massive ($4 \times 10^{10} < M_\star/M_\odot \lesssim 1 \times 10^{11}$) in regions with relatively low surface density, while galaxies with $f_{\rm gas} \lesssim 0.5$ are more massive ($\gtrsim 1 \times 10^{11}$) and in regions with higher surface density.
6. Massive main-sequence galaxies in the protocluster may be evolving under the effect of the specific environment. A systematically different correlation between SFE versus stellar mass might be the combined result of a higher gas volume density and the non-negligible contribution of dark matter imprinted in the surface number density (and CO line widths), but a quantitative assessment should be performed in future studies to confirm this hypothesis.

The sample size is still small to discuss statistical significance as a general picture of galaxy evolution. Furthermore, the different methods used in the derivation of parameters other than $M_{\rm gas}$, i.e., SFR and $M_\star$, when comparing field samples. Therefore, larger surveys are necessary to probe a wide range of characteristic environments (e.g., diverse galaxy number densities) and redshifts that can be constructed with the same analysis tools. Deeper observations are also necessary to investigate the evolution of less massive galaxies and their connection to the probed massive galaxies on the protocluster.

We are immensely grateful to the anonymous referee for constructive comments that greatly improved the quality and the clarity of this work. We thank Nick Scoville for the suggestion of testing dust detection with various resolutions, which improved our analysis quality. This paper makes use of the following ALMA data: ADS/JAO.ALMA#2012.1.00242.S. ALMA is a partnership of ESO (representing its member states), NSF (USA), and NINS (Japan), together with NRC (Canada) and NSC and ASIAA (Taiwan) and KASI (Republic of Korea), in cooperation with the Republic of Chile. The Joint ALMA Observatory is operated by ESO, AUI/NRAO, and NAOJ. M.L. was supported by the ALMA Japan Research Grant of NAOJ Chile Observatory, NAOJ-ALMA-169. M.L. and T.S. were financially supported by a Research Fellowship from the Japan Society for the Promotion of Science for Young Scientists. R.K. and Y.T. were supported by a JSPS Grant-in-Aid for Scientific Research (A) Number 15H02073. K.K. was supported by JSPS Grant-in-Aid for Scientific Research (A) Number 25247019. T.K. is financially supported by Grant-in-Aid for Scientific

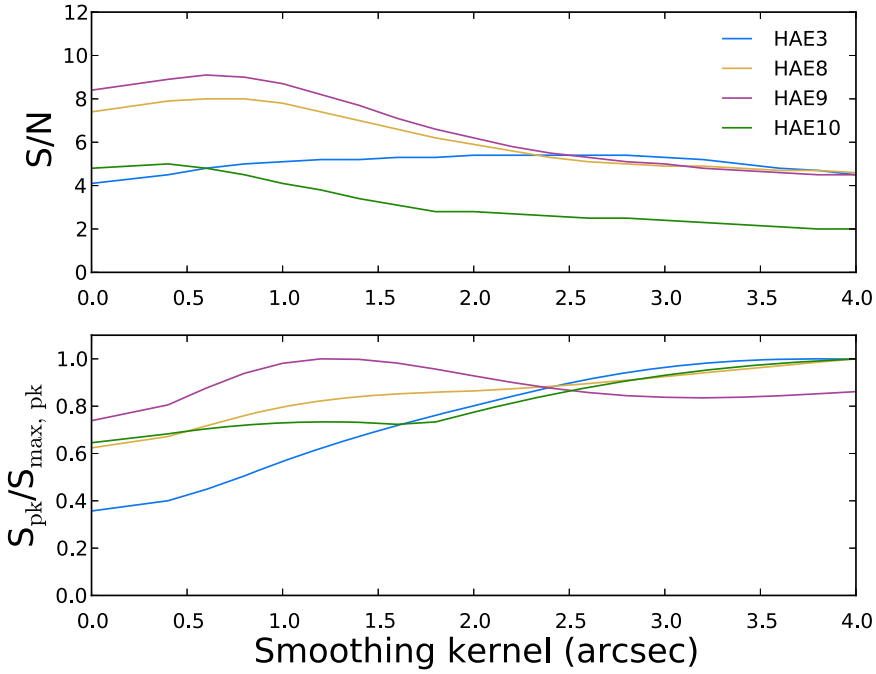

Figure 15. Same growth curve as in Figure 14 but for Band 6. Again, although the peak flux is recovered less with the adopted kernel of 0.″8, they have a low S/N, suggesting large uncertainties are also clearly included in the brightest peak.

Research (JP21340045 and JP24244015) from the Japanese Ministry of Education, Culture, Sports and Science. Data analysis was in part carried out on the open use data analysis computer system at the Astronomy Data Center, ADC, of the National Astronomical Observatory of Japan.

Facilities: ALMA, ASTE (AzTEC), *Spitzer* (MIPS), *Subaru* (MOIRCS).

Software: CASA (McMullin et al. 2007), Astropy (Astropy Collaboration et al. 2013).

Appendix A
Flux versus S/N

We also checked whether the peak flux is consistent with other flux measurements, i.e., Gaussian fitting (using CASA commend `imfit`) and aperture photometry that is clipped below the 2.6σ. For the CO (3–2) measurement, we also tested the spectra-based fitting by integrating the spectrum by using CASA `specfit`, if it is available for each smoothed image. All data are measured from the primary-beam-corrected maps. Furthermore, except for HAE16 in Band 6, all of the sources are within a good sensitivity region. While some compact sources (in the original image) with a high S/N ($\sim$10) have peak flux values consistent with those of other methods, the relatively low S/N (S/N $\leqslant$ 7) with extended ALMA detections do not ensure that a Gaussian fitting is a secure method. Therefore, taking a peak flux would be a more robust method to maximize the S/N and consider a galaxy as an unresolved source.

We investigate the growth curve of a galaxy to optimize the smoothing kernel and then to estimate a flux (Figures 14 and 15). The growth curve gradually approaches the maximum value, while the S/N reaches a peak and then decreases as the noise level increases and the smoothing Gaussian kernel becomes larger. In some cases, the peak flux decreases after it has reached a peak because of contamination in side-lobes in interferometric data sets or contamination from nearby galaxies (on the map). Smoothing major axis = 0.0 implies no smoothing. We tested growth curves using kernels of 0.″4 to 4.″0 in steps of 0.″2 (convolved beam size = 0.8 to 4.1) for Band 6 and 0.6 to 4.0 for Band 3 (convolved beam size = $\sim$0.″9 to 4.″1). Combining all the growth curves in Band 3 and Band 6, we decided to use the Gaussian kernel of 0.″8 for Band 6 and 0.″6 for Band 3.

Appendix B
Position Error

We investigated the peak poisition consistency between the Hα position (I. Tanaka et al. 2017, in preparation) and CO (3–2) or 1.1 mm. The observations have a similar resolution of $\sim$0.″7–0.″9. Figure 16 shows how far the peak position is offset in CO (3–2) and 1.1 mm images with respect to the NB position. The position error expected from the interferometric data depends on the S/N and synthesized beam size. The expected position error is $\sim$0.″1. More errors that could be associated with the phase error in the phase calibrator may be added. Compared to this, the position accuracy for NB compared to 2MASS is 0.″044 (I. Tanaka et al. 2017, in preparation).

While we conclude that the position is roughly consistent with each other within $\sim$0.″4 resolution, we note that there might be a systematic offset in the peak position of CO(3–2) and 1.1 mm compared to the Hα peak (on average $\sim$0.″2). The source with the highest offset is HAE4 (see also Figure 4; the distribution of Hα is extended compared to the distribution of CO(3–2) or 1.1 mm). The position difference between the Hα, CO (3–2) and 1.1 mm, therefore, appears to originate from the difference in the internal structure of a galaxy and/or the effect of dust extinction. Further discussion should be conducted with a higher resolution and high sensitivity observation.

Appendix C
Dynamical Mass Problem

While being a fairly crude estimation, we compare a dynamical mass with the sum of the stellar mass, gas, and dark-matter (DM)

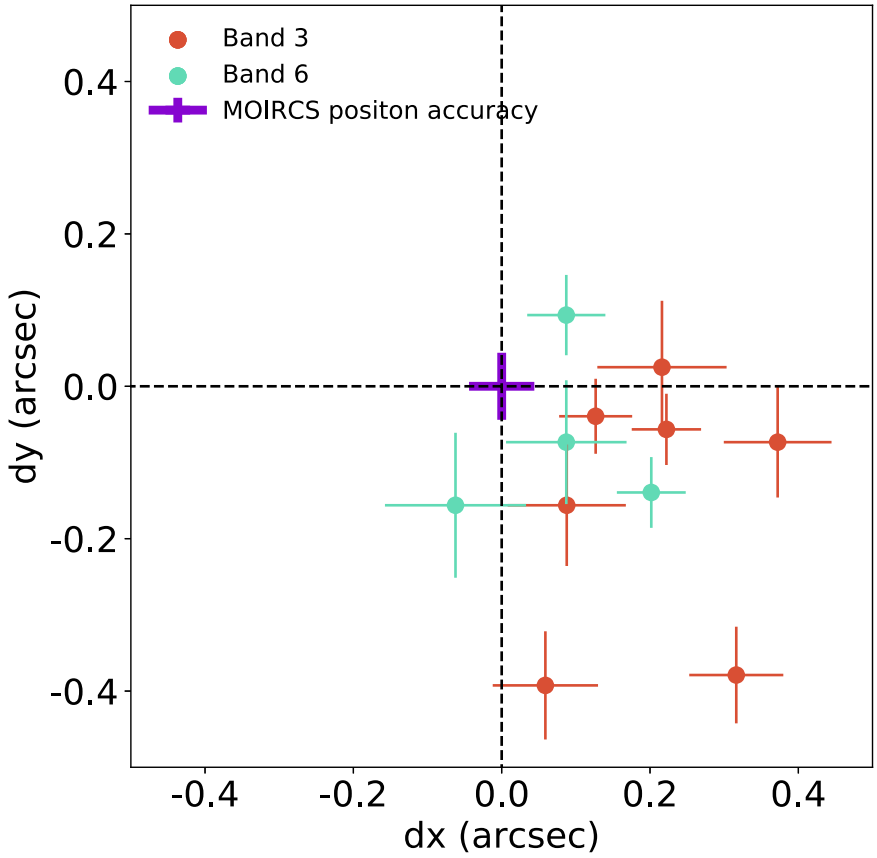

Figure 16. Position offset with respect to the NB catalog. We find that the position is roughly consistent with each other within $\sim 0\farcs4$. Torquoise circles indicate Band 6 1.1 mm observations and crimson circles indicate Band 3 CO (3–2) observations.The position accuracy for NB compared to 2MASS is $0\farcs044$ (I. Tanaka et al. 2017, in preparation).

mass, to impose a limit on the conversion factor. We estimate the dynamical mass by taking an average of two different estimators (i.e., an isotropic virial estimator and a rotating disk estimator; Tacconi et al. 2008; Tan et al. 2014). Both estimators scale the dynamical mass as a linear function of the galaxy size. We adopt a size larger by a factor of two ($r_e = 10$ kpc) than compared to the typical CO(3–2) size of a star-forming galaxy at $z \sim 2$ ($r_e = 5$ kpc; e.g., Tacconi et al. 2013; Bolatto et al. 2015). The exact size measurement will be presented in a subsequent paper, but the assumption adopted here is meant to provide one of the representative cases in our sample that are on the main sequence but require a lower conversion factor. In other words, the assumption provides upper limits of the dynamical mass, thereby placing upper limits on the conversion factor. Without quantitatively addressing the size measurements, there are several supportive aspects for the assumption. First, most sources are unresolved in CO (3–2), Hα, and the stellar component, with a resolution of $0\farcs7 - 0\farcs9$. Therefore, most of them presumably have (as of visual inspection) $r_e \lesssim 10$ kpc. Second, it is known that galaxy sizes measured from rest-frame UV and optical spectra (which trace a star-forming region and stellar component, respectively) decrease with increasing redshift (e.g., Trujillo et al. 2007; van der Wel et al. 2014); therefore, we do not expect extremely large ($r_e > 10$ kpc) massive galaxies at such high redshift even if we take into account the size–mass relation. Third, the CO measurements in Tacconi et al. (2008) and Bolatto et al. (2015) suggest that the gas distribution in both CO(3–2) and CO (1–0) is comparable to those observed from rest-frame UV and optical bands. Our visual inspection also supports such a picture (i.e., it rules out the argument that the sizes are significantly different from each other), but it could be the case that the CO (3–2) size is larger than the compact ($r_e \lesssim 1$ kpc) stellar component. Finally, although there are some arguments regarding the effect of the environment on the size difference particularly for high-z clusters, in the case of quiescent early-type galaxies (e.g., Rettura et al. 2010; Raichoor et al. 2012; Delaye et al. 2014) and perhaps larger sizes in star-forming galaxies compared to those in general fields selected as Lyman-break galaxies (M. Kubo et al. 2017, in private communication), the derived galaxy sizes are still not extreme cases with $r_e > 10$ kpc. For the DM mass estimation included within r_e, we adopt a nominal value of 0.25 $M_{\rm dyn}$ (Daddi et al. 2010).[26] We used the line widths listed in Table 1, which are likely the upper limits of FWHM that yield the highest S/N when integrating across the velocity range (following Seko et al. 2016; M. Lee et al. 2017, in preparation). Since we cannot constrain the inclination of the galaxy from the measurement, substantial uncertainties are included in the estimation of true line width. Nevertheless, more than half of the line widths already exceed 400 km s^{-1}; therefore, we may be observing these galaxies edge-on, rather than face-on, for the disk structure. Otherwise, they must be extremely unstable. We found the median dynamical mass $M_{\rm dyn} \sim 5 \times 10^{11}\ M_\odot$, and the masses of two out of seven HAEs (HAE5 and HAE8) are within the effective radius

[26] See also Wuyts et al. (2016) for a slightly higher value or Price et al. (2016) for a smaller value; all the values are in the range of $M_{\rm DM} \simeq (0.1\text{–}0.3) \times M_{\rm dyn}$, and we note that two recent studies have estimated the gas mass without direct measurement and instead with scaling relations. In any case, the dark matter is less likely to be the dominant component within the effective radius.

$(=(M_\star + M_{\rm gas})/2)$, which already exceeds the estimated dynamical mass without considering the DM contribution, if we adopt the "Galactic" conversion factor $\alpha_{\rm CO} = 4.36$ (corrected for helium) or an even higher value of $\alpha_{\rm CO} = 6.5$ as suggested in Scoville et al. (2016). The two galaxies have the lowest line widths. Our measurements may underestimate the dynamical mass within the effective radius. If we adopt a loose constraint on the size, $r_e = 6$ kpc, HAE4 would also be a galaxy that cannot be explained by the dynamical estimator. Although the uncertainty included in the measurements is large, we caution that some galaxies might tend to reduce the conversion factor below the assumed value.

References

Alatalo, K., Appleton, P. N., Lisenfeld, U., et al. 2015, ApJ, 812, 117
Appleton, P. N., Guillard, P., Boulanger, F., et al. 2013, ApJ, 777, 66
Astropy Collaboration, Robitaille, T. P., Tollerud, E. J., et al. 2013, A&A, 558, A33
Baldry, I. K., Glazebrook, K., Brinkmann, J., et al. 2004, ApJ, 600, 681
Balogh, M. L., Schade, D., Morris, S. L., et al. 1998, ApJL, 504, L75
Berta, S., Lutz, D., Genzel, R., Förster-Schreiber, N. M., & Tacconi, L. J. 2016, A&A, 587, A73
Best, P. N., Lehnert, M. D., Miley, G. K., & Röttgering, H. J. A. 2003, MNRAS, 343, 1
Blanton, M. R., Eisenstein, D., Hogg, D. W., Schlegel, D. J., & Brinkmann, J. 2005, ApJ, 629, 143
Blanton, M. R., & Moustakas, J. 2009, ARA&A, 47, 159
Blundell, K. M., & Fabian, A. C. 2011, MNRAS, 412, 705
Bolatto, A. D., Warren, S. R., Leroy, A. K., et al. 2015, ApJ, 809, 175
Bolatto, A. D., Wolfire, M., & Leroy, A. K. 2013, ARA&A, 51, 207
Boselli, A., Cortese, L., Boquien, M., et al. 2014, A&A, 564, A67
Bruzual, G., & Charlot, S. 2003, MNRAS, 344, 1000
Bullock, J. S., Kolatt, T. S., Sigad, Y., et al. 2001, MNRAS, 321, 559
Butcher, H., & Oemler, A., Jr. 1978, ApJ, 219, 18
Butcher, H., & Oemler, A., Jr. 1984, ApJ, 285, 426
Carilli, C. L., & Walter, F. 2013, ARA&A, 51, 105
Casey, C. M. 2016, ApJ, 824, 36
Chamaraux, P., Balkowski, C., & Gerard, E. 1980, A&A, 83, 38
Chapman, S. C., Bertoldi, F., Smail, I., et al. 2015, MNRAS, 449, L68
Chiang, Y.-K., Overzier, R., & Gebhardt, K. 2013, ApJ, 779, 127
Chiang, Y.-K., Overzier, R. A., Gebhardt, K., et al. 2015, ApJ, 808, 37
Chung, A., van Gorkom, J. H., Kenney, J. D. P., Crowl, H., & Vollmer, B. 2009, AJ, 138, 1741
Cicone, C., Maiolino, R., Sturm, E., et al. 2014, A&A, 562, A21
Cooke, E. A., Hatch, N. A., Stern, D., et al. 2016, ApJ, 816, 83
Cortese, L., Minchin, R. F., Auld, R. R., et al. 2008, MNRAS, 383, 1519
Cybulski, R., Yun, M. S., Erickson, N., et al. 2016, MNRAS, 459, 3287
da Cunha, E., Walter, F., Smail, I. R., et al. 2015, ApJ, 806, 110
Daddi, E., Bournaud, F., Walter, F., et al. 2010, ApJ, 713, 686
Daddi, E., Dannerbauer, H., Elbaz, D., et al. 2008, ApJL, 673, L21
Daddi, E., Dannerbauer, H., Liu, D., et al. 2015, A&A, 577, A46
Daddi, E., Dickinson, M., Morrison, G., et al. 2007, ApJ, 670, 156
Darvish, B., Mobasher, B., Sobral, D., et al. 2016, ApJ, 825, 113
Das, M., Saito, T., Iono, D., Honey, M., & Ramya, S. 2015, ApJ, 815, 40
Davé, R., Finlator, K., & Oppenheimer, B. D. 2011, MNRAS, 416, 1354
De Breuck, C., Bertoldi, F., Carilli, C., et al. 2004, A&A, 424, 1
Decarli, R., Walter, F., Aravena, M., et al. 2016a, ApJ, 833, 69
Decarli, R., Walter, F., Aravena, M., et al. 2016a, ApJ, 833, 70
Delaye, L., Huertas-Company, M., Mei, S., et al. 2014, MNRAS, 441, 203
Dickman, R. L., Snell, R. L., & Schloerb, F. P. 1986, ApJ, 309, 326
Domínguez, A., Siana, B., Henry, A. L., et al. 2013, ApJ, 763, 145
Dressler, A. 1980, ApJ, 236, 351
Dressler, A., Oemler, A., Jr., Couch, W. J., et al. 1997, ApJ, 490, 577
Elbaz, D., Dickinson, M., Hwang, H. S., et al. 2011, A&A, 533, A119
Emonts, B. H. C., Feain, I., Röttgering, H. J. A., et al. 2013, MNRAS, 430, 3465
Emonts, B. H. C., Lehnert, M. D., Villar-Martín, M., et al. 2016, Sci, 354, 1128
Galametz, A., Stern, D., De Breuck, C., et al. 2012, ApJ, 749, 169
Garn, T., & Best, P. N. 2010, MNRAS, 409, 421
Geach, J. E., Smail, I., Best, P. N., et al. 2008, MNRAS, 388, 1473
Gehrels, N. 1986, ApJ, 303, 336
Genzel, R., Tacconi, L. J., Combes, F., et al. 2012, ApJ, 746, 69
Genzel, R., Tacconi, L. J., Lutz, D., et al. 2015, ApJ, 800, 20
Hatch, N. A., Kurk, J. D., Pentericci, L., et al. 2011, MNRAS, 415, 2993
Hayashi, M., Kodama, T., Tanaka, I., et al. 2016, ApJL, 826, L28
Hodge, J. A., Karim, A., Smail, I., et al. 2013, ApJ, 768, 91
Ibar, E., Sobral, D., Best, P. N., et al. 2013, MNRAS, 434, 3218
Ichikawa, T., Suzuki, R., Tokoku, C., et al. 2006, Proc. SPIE, 6269, 626916
Kajisawa, M., Kodama, T., Tanaka, I., Yamada, T., & Bower, R. 2006, MNRAS, 371, 577
Kauffmann, G., White, S. D. M., Heckman, T. M., et al. 2004, MNRAS, 353, 713
Keating, G. K., Marrone, D. P., Bower, G. C., et al. 2016, ApJ, 830, 34
Kennicutt, R. C., & Evans, N. J. 2012, ARA&A, 50, 531
Kennicutt, R. C., Jr. 1998, ApJ, 498, 541
Knopp, G. P., & Chambers, K. C. 1997, ApJS, 109, 367
Kodama, T., Hayashi, M., Koyama, Y., et al. 2015, in IAU Symp. 309, Galaxies in 3D across the Universe, ed. B. L. Ziegler (Cambridge: Cambridge Univ. Press), 255
Koyama, Y., Kodama, T., Tadaki, K.-i., et al. 2014, ApJ, 789, 18
Koyama, Y., Smail, I., Kurk, J., et al. 2013, MNRAS, 434, 423
Kulas, K. R., McLean, I. S., Shapley, A. E., et al. 2013, ApJ, 774, 130
Kurczynski, P., Gawiser, E., Acquaviva, V., et al. 2016, ApJL, 820, L1
Kurk, J., Cimatti, A., Zamorani, G., et al. 2009, A&A, 504, 331
Kurk, J. D., Röttgering, H. J. A., Pentericci, L., et al. 2000, A&A, 358, L1
Lagache, G., Dole, H., Puget, J.-L., et al. 2004, ApJS, 154, 112
Lagos, C. D. P., Baugh, C. M., Lacey, C. G., et al. 2011, MNRAS, 418, 1649
Lagos, C. d. P., Bayet, E., Baugh, C. M., et al. 2012, MNRAS, 426, 2142
Le Fevre, O., Deltorn, J. M., Crampton, D., & Dickinson, M. 1996, ApJL, 471, L11
Lee, M., Suzuki, K., Kohno, K., et al. 2015, in IAU Symp. 309, Galaxies in 3D across the Universe, ed. B. L. Ziegler (Cambridge: Cambridge Univ. Press), 287
Lee, N., Sanders, D. B., Casey, C. M., et al. 2015, ApJ, 801, 80
Lehmer, B. D., Lucy, A. B., Alexander, D. M., et al. 2013, ApJ, 765, 87
Leon, S., Combes, F., & Menon, T. K. 1998, A&A, 330, 37
Madau, P., & Dickinson, M. 2014, ARA&A, 52, 415
Magdis, G. E., Daddi, E., Béthermin, M., et al. 2012, ApJ, 760, 6
Mannucci, F., Cresci, G., Maiolino, R., Marconi, A., & Gnerucci, A. 2010, MNRAS, 408, 2115
Mayo, J. H., Vernet, J., De Breuck, C., et al. 2012, A&A, 539, A33
McMullin, J. P., Waters, B., Schiebel, D., Young, W., & Golap, K. 2007, adass XVI, 376, 127
Mo, H. J., Mao, S., & White, S. D. M. 1998, MNRAS, 295, 319
Mok, A., Wilson, C. D., Golding, J., et al. 2016, MNRAS, 456, 4384
Muldrew, S. I., Hatch, N. A., & Cooke, E. A. 2015, MNRAS, 452, 2528
Noeske, K. G., Weiner, B. J., Faber, S. M., et al. 2007, ApJL, 660, L43
Obreschkow, D., Heywood, I., Klöckner, H.-R., & Rawlings, S. 2009, ApJ, 702, 1321
Obreschkow, D., & Rawlings, S. 2009, ApJL, 696, L129
Orsi, Á. A., Fanidakis, N., Lacey, C. G., & Baugh, C. M. 2016, MNRAS, 456, 3827
Oteo, I., Sobral, D., Ivison, R. J., et al. 2015, MNRAS, 452, 2018
Overzier, R. A., Miley, G. K., Bouwens, R. J., et al. 2006, ApJ, 637, 58
Peng, Y.-j., Lilly, S. J., Kovač, K., et al. 2010, ApJ, 721, 193
Planck Collaboration, Ade, P. A. R., Aghanim, N., et al. 2015, A&A, 582, A29
Poggianti, B. M., Desai, V., Finn, R., et al. 2008, ApJ, 684, 888
Price, S. H., Kriek, M., Shapley, A. E., et al. 2016, ApJ, 819, 80
Raichoor, A., Mei, S., Stanford, S. A., et al. 2012, ApJ, 745, 130
Rettura, A., Rosati, P., Nonino, M., et al. 2010, ApJ, 709, 512
Riechers, D. A., Capak, P. L., Carilli, C. L., et al. 2010, ApJL, 720, L131
Rigby, J. R., Marcillac, D., Egami, E., et al. 2008, ApJ, 675, 262
Rocca-Volmerange, B., Le Borgne, D., De Breuck, C., Fioc, M., & Moy, E. 2004, A&A, 415, 931
Roettgering, H. J. A., van Ojik, R., Miley, G. K., et al. 1997, A&A, 326, 505
Saintonge, A., Lutz, D., Genzel, R., et al. 2013, ApJ, 778, 2
Saito, T., Iono, D., Yun, M. S., et al. 2015, ApJ, 803, 60
Sakamoto, K., Aalto, S., Costagliola, F., et al. 2013, ApJ, 764, 42
Sargent, M. T., Daddi, E., Béthermin, M., et al. 2014, ApJ, 793, 19
Schinnerer, E., Groves, B., Sargent, M. T., et al. 2016, ApJ, 833, 112
Schmidt, M. 1959, ApJ, 129, 243
Scoville, N., Aussel, H., Sheth, K., et al. 2014, ApJ, 783, 84
Scoville, N., Lee, N., Vanden Bout, P., et al. 2017, ApJ, 837, 150
Scoville, N., Sheth, K., Aussel, H., et al. 2016, ApJ, 820, 83
Seko, A., Ohta, K., Yabe, K., et al. 2016, ApJ, 819, 82
Serra, P., Oosterloo, T., Morganti, R., et al. 2012, MNRAS, 422, 1835
Seymour, N., Stern, D., De Breuck, C., et al. 2007, ApJS, 171, 353
Shimakawa, R., Kodama, T., Tadaki, K.-i., et al. 2015, MNRAS, 448, 666

Shivaei, I., Kriek, M., Reddy, N. A., et al. 2016, ApJL, 820, L23
Shivaei, I., Reddy, N., Shapley, A., et al. 2017, ApJ, 837, 157
Sobral, D., Best, P. N., Geach, J. E., et al. 2009, MNRAS, 398, 75
Sobral, D., Best, P. N., Matsuda, Y., et al. 2012, MNRAS, 420, 1926
Sobral, D., Best, P. N., Smail, I., et al. 2014, MNRAS, 437, 3516
Solomon, P. M., Downes, D., Radford, S. J. E., & Barrett, J. W. 1997, ApJ, 478, 144
Solomon, P. M., Rivolo, A. R., Barrett, J., & Yahil, A. 1987, ApJ, 319, 730
Solomon, P. M., & Vanden Bout, P. A. 2005, ARA&A, 43, 677
Speagle, J. S., Steinhardt, C. L., Capak, P. L., & Silverman, J. D. 2014, ApJS, 214, 15
Steidel, C. C., Rudie, G. C., Strom, A. L., et al. 2014, ApJ, 795, 165
Strazzullo, V., Gobat, R., Daddi, E., et al. 2013, ApJ, 772, 118
Tacconi, L. J., Genzel, R., Saintonge, A., et al. 2017, arXiv:1702.01140
Tacconi, L. J., Genzel, R., Smail, I., et al. 2008, ApJ, 680, 246
Tacconi, L. J., Neri, R., Genzel, R., et al. 2013, ApJ, 768, 74
Tadaki, K.-i., Genzel, R., Kodama, T., et al. 2017, ApJ, 834, 135
Tadaki, K.-i., Kodama, T., Tamura, Y., et al. 2014, ApJL, 788, L23
Tadaki, K.-i., Kodama, T., Tanaka, I., et al. 2013, ApJ, 778, 114
Tan, Q., Daddi, E., Magdis, G., et al. 2014, A&A, 569, A98
Tanaka, I., De Breuck, C., Kurk, J. D., et al. 2011, PASJ, 63, 415
Toshikawa, J., Kashikawa, N., Overzier, R., et al. 2014, ApJ, 792, 15
Tran, K.-V. H., Nanayakkara, T., Yuan, T., et al. 2015, ApJ, 811, 28
Trujillo, I., Conselice, C. J., Bundy, K., et al. 2007, MNRAS, 382, 109
Umehata, H., Tamura, Y., Kohno, K., et al. 2015, ApJL, 815, L8
Umehata, H., Tamura, Y., Kohno, K., et al. 2017, ApJ, 835, 98
Valentino, F., Daddi, E., Strazzullo, V., et al. 2015, ApJ, 801, 132
van der Wel, A., Franx, M., van Dokkum, P. G., et al. 2014, ApJ, 788, 28
Venemans, B. P., Röttgering, H. J. A., Miley, G. K., et al. 2007, A&A, 461, 823
Verdes-Montenegro, L., Yun, M. S., Williams, B. A., et al. 2001, A&A, 377, 812
Vulcani, B., Poggianti, B. M., Finn, R. A., et al. 2010, ApJL, 710, L1
Walter, F., Decarli, R., Sargent, M., et al. 2014, ApJ, 782, 79
Wetzel, A. R., Tinker, J. L., & Conroy, C. 2012, MNRAS, 424, 232
Whitaker, K. E., Franx, M., Leja, J., et al. 2014, ApJ, 795, 104
Whitaker, K. E., van Dokkum, P. G., Brammer, G., & Franx, M. 2012, ApJL, 754, L29
Wuyts, E., Kurk, J., Förster Schreiber, N. M., et al. 2014, ApJL, 789, L40
Wuyts, S., Förster Schreiber, N. M., Wisnioski, E., et al. 2016, ApJ, 831, 149
Yun, M. S., Aretxaga, I., Gurwell, M. A., et al. 2015, MNRAS, 454, 3485